Simulating shallow morphodynamic flows on evolving topographies

5 authors, including:

Mark J. Woodhouse
University of Bristol
29 PUBLICATIONS **682** CITATIONS

SEE PROFILE

Luke T. Jenkins
University of Bristol
10 PUBLICATIONS **75** CITATIONS

SEE PROFILE

Simulating shallow morphodynamic flows on evolving topographies

Jake Langham[1], Mark J. Woodhouse[2], Andrew J. Hogg[1], Luke T. Jenkins[2] and Jeremy C. Phillips[2]

[1]School of Mathematics, Fry Building, University of Bristol, BS8 1UG, UK
[2]School of Earth Sciences, Wills Memorial Building, University of Bristol, Bristol, BS8 1RJ, UK

We derive general depth-integrated model equations for overland flows featuring the evolution of suspended sediment that may be eroded from or deposited onto the underlying topography ('morphodynamics'). The resulting equations include geometric corrections that account for large variations in slope angle. These are often non-negligible for Earth-surface flows and may consequently be important for simulating natural hazards. We also show how to adapt existing finite volume schemes for the classical shallow water equations, to simulate our new equations in a way that preserves uniform steady states and exactly conserves the combined mass of the flow and bed. Finally, to demonstrate our formulation, we present computations using simple example model closures, fed by point flux sources. On initially constant slopes, flows exhibit different behaviours depending on the grade. Shallow slopes lead to weakly morphodynamic spreading flows that agree well with analytical similarity solutions. On more severe slopes, rapid erosion occurs, leading to self-channelising flows and ultimately a 'super-erosive' state, in which sediment entrainment and gravitational acceleration perpetually reinforce each other.
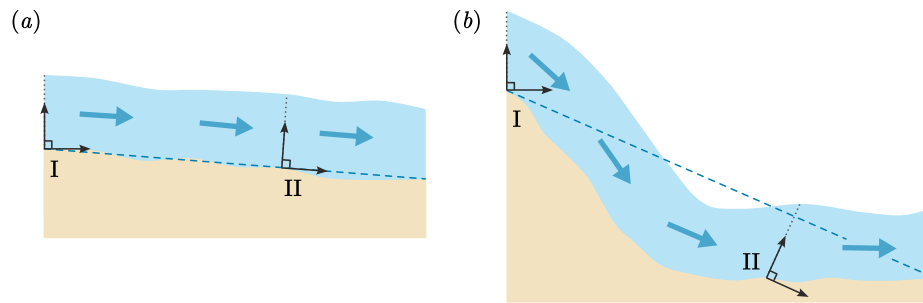
Figure 1. Shallow flows featuring (*a*) small and (*b*) large ranges of slope angles. The black arrows labelled show orthogonal coordinate frames that are (I) aligned with gravity and (II) the mean slope (plotted in dashed blue). Blue arrows indicate the direction of the mean flow velocity.

1. Introduction

Overland flows of water mixed with sediment and debris represent one of the Earth surface's primary hazards [1–3]. Such flows enhance their destructive potential by entraining bed material which is later deposited downstream [4,5]. In many cases, the basal surface can be dramatically reshaped by the flow over its lifespan. Since flows are guided by the topography that they propagate over, there is a mutual coupling between the flow and its bed that becomes particularly important in highly energetic regimes, where large volumes of sediment are mobilised by the flow. Consequently, there is a pressing need for accurate and reliable large-scale flow models of these systems that incorporate the so-called 'morphodynamic' processes of sediment erosion and deposition.

Many authors have proposed extensions to the classical shallow water equations in order to account for the particular physics of mixed-sediment morphodynamic flows [6–19]. These depth-averaged models are a promising step towards achieving truly predictive debris flow simulations that may be relied upon for hazards assessment [20–24] and for estimating physical impacts to the built environment [25,26]. However, it is now known that many common morphodynamic formulations are mathematically ill posed as initial value problems [27,28], which renders them useless as potential tools for hazards prediction, since simulations of ill-posed models cannot be converged to obtain reliable high resolution reference solutions. Moreover, as Iverson and Ouyang note in their detailed review [29], most prior efforts to produce models have contained systemic errors in their mathematical derivations. A particular technical challenge is to account for geometric effects of the underlying topography in a way that is consistent with the coordinates used in depth-averaging. To see why, consider the sketches in Fig. 1. Panel (*a*) depicts flow on a mild slope with relatively small variations in its basal gradient—a typical configuration encountered in applications including river dynamics and hydraulic engineering. Two orthonormal frames are commonly used to derive shallow-layer equations in this setting: (I) gravity aligned axes and (II) mean slope aligned axes. Either frame is suitable for depth-averaging, since in both cases the streamwise axis is roughly parallel to the mean flow. Conversely, the right-hand diagram [Fig. 1(*b*)] portrays the situation for many debris flows, which are initiated on steep slopes before running out onto flatter terrain. Averaging the governing equations with respect to either frame will introduce systematic errors in locations where the mean flow and coordinate axes are misaligned.

Though multiple frameworks exist which resolve this issue in classical shallow water models [30–36], these have largely not been generalised to include the effect of basal topography that is morphodynamically coupled to the flow. An exception is Bouchut *et al.* [37], who have developed shallow morphodynamic avalanche models in one spatial dimension, for both arbitrary basal topographies and reduced cases where slope angle variation and bed dynamics are the same order as the flow depth.

Even in the non-morphodynamic case, models that include these geometric effects appear to have so far made little to no impact on operational debris flow modelling in mountainous regions in the past few decades, despite the fact that these flows necessarily propagate over undulating terrains with large variations in slope angle. This is likely in part due to the additional complexity that the governing equations must feature, as well as the need to specialise models for particular settings. The recent work of Peruzzetto *et al.* [36] has made significant progress in both of these regards, by deriving a non-morphodynamic shallow debris flow model with curvature terms and showing that it is feasible to numerically solve it in settings relevant for hazards simulations.

The work in this paper divides into three parts. Firstly, in Sec. 2 we develop well-posed depth-averaged morphodynamic model equations for debris flows in two spatial dimensions in a way that accounts for large and time-dependent variations in topographic slope angle. While part of our aim is to progress the theoretical advances of previous studies, we place primary focus on obtaining and implementing a framework that is practical for operational use. To this end, restrictions are imposed on both the curvature and dynamics of the bed to obtain a generic and relatively straightforward system that may be specialised to particular flows through the selection of closures specifying the rheology and morphodynamics.

Secondly, in Sec. 3, we show how to solve our equations numerically, by adapting existing finite volume shallow water schemes. This is made convenient by use of an operator splitting approach, which separates the hydraulic evolution of the flow and the morphodynamics, so that relatively few adjustments need to be made to the flow solver itself. Although many studies have already described schemes for the current crop of shallow morphodynamic models [7,9–11,13–18,38–44], we identify and overcome specific issues that must be accounted for when these models are extended to include more geometrical information. Particular care is taken to obtain a scheme that exactly conserves mass—a consideration which is somewhat subtle in our framework because local volume elements depend on the slope angle. When time-stepping the morphodynamics, this amounts to ensuring that any change in the bed volume corresponds exactly with material added to or deposited from the flow. An auxiliary correction algorithm preserves the positivity of the flow depth and solids concentration in cases of rapid sediment deposition. Furthermore, we adapt the approach of Kurganov and Petrova [45], to exactly compute steady states, including stationary solutions (so-called 'lake-at-rest' states). Such schemes are often referred to as 'well balanced'. Numerical solvers which fail to compute these states accurately generate spurious momentum from static initial conditions and may even begin to erode the topography as a result.

Finally, to demonstrate the success of our approach, in Sec. 4 we present some illustrative results. Ideally, numerical methods should be tested by comparing their outputs with analytical reference solutions. However, closed-form solutions are difficult to obtain in most circumstances when morphodynamics is present. Nevertheless, for flows from point sources on planes of initially constant gradient that feature only weak erosion, we derive similarity solutions and confirm that our numerical results agree with them when slopes are mild. On steeper slopes, erosion becomes more rapid and can cause flows to self-channelise. When slopes are extreme, flows ultimately enter a regime where the mutual coupling of sediment entrainment and forcing from the weight of the mixture forms a self-perpetuating cycle that accelerates the flow. We also briefly demonstrate flow on a surface that features a slope transition between two different gradients and note that its behaviour can be largely understood by combining insights from the milder and steeper constant-slope regimes.

2. Derivation of the governing equations

We consider a well-mixed flow of fluid and solid particles, propagating over an erodible substrate, featuring mass transfer between the flow and its underlying bed. The particles are assumed to be monodisperse and small, relative to the flow length scales, so that both fluid and solid phases may be modelled as continua. Moreover, we suppose that the substrate is static and homogeneously composed of the same materials as the flow, with the solid particles occupying a constant fraction

ψ_b of its volume. The densities of fluid and solids are denoted by ρ_f and ρ_s respectively. Then, the total density field for the mixture is $\rho = \psi \rho_s + (1 - \psi)\rho_f$, where ψ is the scalar field quantifying the volume fraction of solids in the flow. A velocity field for the mixture may be defined by summing the contributions of each fraction to the bulk momentum:

$$\psi \rho_s \boldsymbol{u}_s + (1 - \psi)\rho_f \boldsymbol{u}_f \equiv \rho \boldsymbol{u}, \tag{2.1}$$

where $\boldsymbol{u}_s$ and $\boldsymbol{u}_f$ denote the velocities of the solid and fluid phases respectively [29].

The phases obey separate conservation laws for their occupying volume and momentum, which may be linearly combined as necessary to obtain governing equations for the mixture. In terms of Cartesian coordinates (x, y, z) (oriented with gravity pointing in the negative z-direction) and time t, we write conservation of bulk mass, solids volume and bulk momentum, as

$$\frac{\partial \rho}{\partial t} + \nabla \cdot (\rho \boldsymbol{u}) = 0, \tag{2.2a}$$

$$\frac{\partial \psi}{\partial t} + \nabla \cdot (\psi \boldsymbol{u}_s) = 0, \tag{2.2b}$$

$$\rho \left[\frac{\partial \boldsymbol{u}}{\partial t} + \boldsymbol{u} \cdot \nabla \boldsymbol{u} \right] + \nabla \cdot \kappa = -\nabla p + \nabla \cdot \tau - \rho \boldsymbol{g}, \tag{2.2c}$$

where $\nabla \equiv (\partial/\partial x, \partial/\partial y, \partial/\partial z)^{\mathsf{T}}$. On the left-hand side of Eq. (2.2c), $\nabla \cdot \kappa$ is momentum transport by the interphase drift velocity $\boldsymbol{u}_s - \boldsymbol{u}_f$, with $\kappa = \rho_s \rho_f \psi (1 - \psi) \rho^{-1} (\boldsymbol{u}_s - \boldsymbol{u}_f) \otimes (\boldsymbol{u}_s - \boldsymbol{u}_f)$. On the right-hand side, p denotes the pressure field of the mixture, τ denotes its deviatoric stress tensor and $\boldsymbol{g} = (0, 0, g)^{\mathsf{T}}$ is gravitational acceleration. We have not included the separate single-phase momentum equations here, since these will not ultimately be required to close our model.

For reference, a schematic of the flow, its geometry, and key variables used in the following derivation, is depicted in Fig. 2. As highlighted in Fig. 2(a), the flowing mixture is bounded below by the bed substrate, whose boundary is given by the surface $F_b(x, y, z, t) \equiv z - b(x, y, t) = 0$. As depicted in Fig. 2(b), this boundary evolves according to morphodynamic processes, which are assumed to act normal to the bed surface, at a rate $M(x, y, t)$. More precisely, we stipulate that F_b moves according to

$$\frac{\partial F_b}{\partial t} - M \boldsymbol{n} \cdot \nabla F_b = 0, \tag{2.3}$$

where $\boldsymbol{n}$ is the outward-pointing unit vector field normal to the bed surface. The sign convention of Eq. (2.3) is that $M(x, y, t) > 0$ implies net erosion and $M(x, y, t) < 0$ implies net deposition. By definition, $\boldsymbol{n} = \nabla F_b / |\nabla F_b|$ and so

$$\boldsymbol{n} = \frac{1}{\gamma} \left(-\frac{\partial b}{\partial x}, -\frac{\partial b}{\partial y}, 1 \right)^{\mathsf{T}}, \quad \text{where} \quad \gamma = \sqrt{1 + \left(\frac{\partial b}{\partial x} \right)^2 + \left(\frac{\partial b}{\partial y} \right)^2}. \tag{2.4}$$

Note that $\gamma = 1/\cos(\vartheta)$, where ϑ is the angle between the local slope normal and gravity. We may then write the equation

$$\frac{\partial b}{\partial t} = -\gamma M, \tag{2.5}$$

for the bed evolution, leaving the morphodynamic rate function M as a general closure that must be specified for particular systems.

Across the bed-flow interface, there are discontinuous jumps in the physical quantities from their assumed basal values, to the flowing state. We label variables evaluated on the immediate flow side of the discontinuity with $^+$ superscripts. Since mass and volume must be conserved over the jump, any motion of the interface must be balanced by corresponding fluxes on the flowing side. From Eqs. (2.2a) and (2.2b), we determine that

$$\rho^+ \boldsymbol{u}^+ \cdot \boldsymbol{n} = (\rho_b - \rho^+)M, \quad \text{and} \quad \psi^+ \boldsymbol{u}_s^+ \cdot \boldsymbol{n} = (\psi_b - \psi^+)M, \tag{2.6a,b}$$

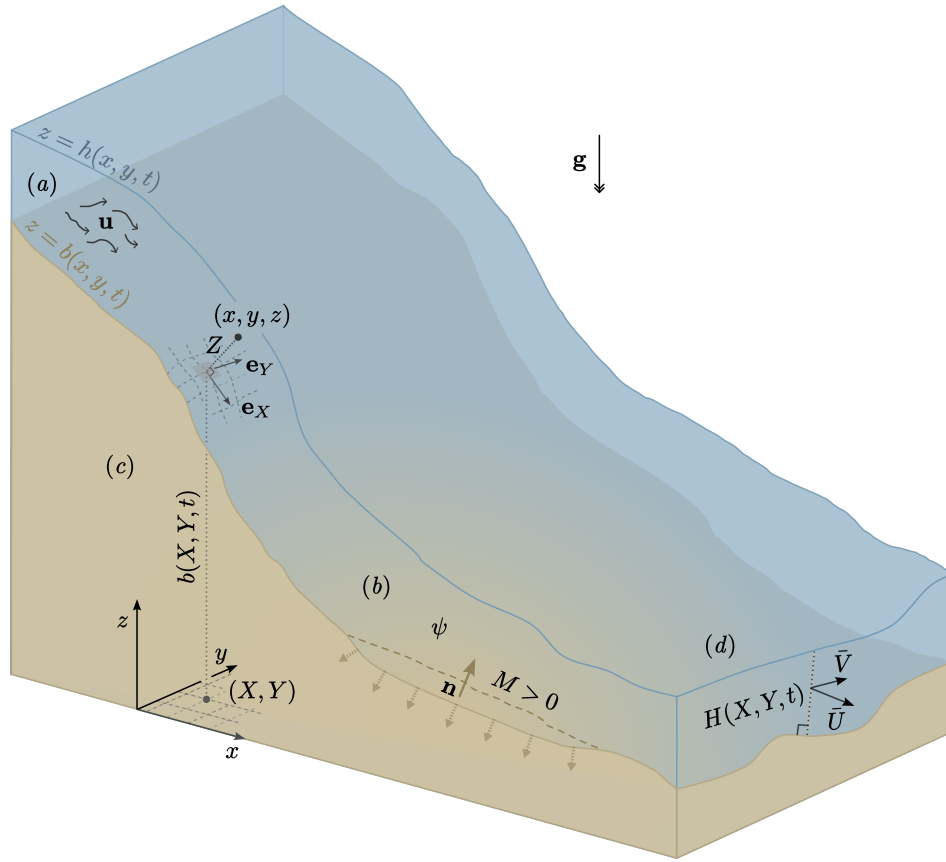where $\rho_b = \psi_b \rho_s + (1 - \psi_b)\rho_f$ is the density of the bed.

Figure 2. Diagram of the flow system, depicting aspects of the model setup and derivation. (*a*) Flow bounding surfaces and the velocity field $\boldsymbol{u}$, which is predominantly oriented parallel to the bed. (*b*) Depiction of morphodynamics. Erosion at rate $M > 0$ extracts a patch material from the bed and adds it to the flow, locally enhancing the solids fraction field ψ and leading to a preferentially concentrated region, as indicated by the surrounding shading of the flow. (*c*) Relationship between Cartesian (x, y, z) and surface-fitted coordinates (X, Y, Z). (*d*) Surface-fitted velocity fields $\bar{U}$ and $\bar{V}$, obtained after averaging over the depth $H(X, Y, t)$, measured along the direction normal to the bed.

The upper boundary of the flow is a free surface with equation $F_h(x, y, z, t) = h(x, y, t) - z = 0$. Since there is no mass transfer across this interface, its boundary is kinematic and evolves according to

$$\frac{\partial F_h}{\partial t} + \boldsymbol{u}|_h \cdot \nabla F_h = 0, \tag{2.7}$$

where $\boldsymbol{u}|_h = \boldsymbol{u}|_{z=h(x,y,t)} \equiv (u_h, v_h, w_h)^\mathsf{T}$. Mechanically, the mixture is stress-free and at atmospheric pressure across this surface. Conservation of fluid and solids volume necessitates $\boldsymbol{u}_s = \boldsymbol{u}_f$ along the flow side of the interface, so this is the only condition required at this boundary.

A shallow-layer model for the flow may be obtained by depth-averaging Eqs. (2.2*a–c*), subject to the boundary conditions (2.6*a,b*) and (2.7), and systematically neglecting fluid accelerations that are perpendicular to the plane of motion. In cases where the bed possesses steep gradients, this means that the leading-order dynamics retains non-negligible vertical acceleration [29]. Moreover, if the topography contains a mixture of steep and shallow grades it is not possible to fix a Cartesian frame such that the motion may be consistently neglected in a particular coordinate direction. Therefore, in order to obtain a model that may be applied for general topographies, we transform to a curvilinear frame that is fitted to the time-dependent bed surface.

Specifically, we rewrite each point in terms of new time-dependent coordinates (X, Y, Z), as

$$\begin{pmatrix} x \\ y \\ z \end{pmatrix} = \begin{pmatrix} X \\ Y \\ b(X, Y, t) \end{pmatrix} + Z\boldsymbol{n}(X, Y, t). \tag{2.8}$$

Note that at each point in time, $Z = 0$ represents a Cartesian parametrisation of the bed surface and the coordinate $Z \geq 0$ gives the perpendicular distance from the bed. The mapping is given diagrammatically in Fig. 2(*c*). It is unique, provided that the local radius of curvature everywhere exceeds the flow depth and that $\boldsymbol{n}$ is everywhere well defined and single valued. Variants and generalisations of this transformation have previously been employed to develop non-morphodynamic shallow-layer models [33–36]. Here, we extend this approach for flows with a time-dependent bed.

The basis vectors $\{\boldsymbol{e}_X, \boldsymbol{e}_Y, \boldsymbol{e}_Z\}$ for the new frame are obtained by differentiating Eq. (2.8):

$$\boldsymbol{e}_X = \begin{pmatrix} 1 \\ 0 \\ \frac{\partial b}{\partial X} \end{pmatrix} + Z\frac{\partial \boldsymbol{n}}{\partial X}, \quad \boldsymbol{e}_Y = \begin{pmatrix} 0 \\ 1 \\ \frac{\partial b}{\partial Y} \end{pmatrix} + Z\frac{\partial \boldsymbol{n}}{\partial Y}, \quad \boldsymbol{e}_Z = \boldsymbol{n}. \tag{2.9a–c}$$

These are time dependent and neither mutually orthogonal, nor unit length. We define A to be the change of basis matrix from Cartesian to the new frame and denote $J = \det(A^{-1})$. We shall write the bulk flow velocity in slope-aligned coordinates as $\boldsymbol{U} = (U, V, W)^\mathsf{T} = A\boldsymbol{u}$ and the solids velocity as $\boldsymbol{U}_s = (U_s, V_s, W_s)^\mathsf{T} = A\boldsymbol{u}_s$. Similarly, the interphase momentum transport and stress tensors are to be denoted as $K = A\kappa A^{-1}$ and $T = A\tau A^{-1}$ respectively. Time derivatives in the new coordinates must be transformed to account for the advection of the reference frame with velocity $\dot{\boldsymbol{X}} \equiv (\partial X/\partial t, \partial Y/\partial t, \partial Z/\partial t)^\mathsf{T}$. By taking the total derivative of Eq. (2.8) with respect to time (i.e. holding the Cartesian coordinates fixed) and rearranging, we compute

$$\dot{\boldsymbol{X}} = -\frac{1}{\gamma}\frac{\partial b}{\partial t}\begin{pmatrix} \frac{\partial b}{\partial X}/\gamma \\ \frac{\partial b}{\partial Y}/\gamma \\ 1 \end{pmatrix} + Z\frac{\mathrm{d}}{\mathrm{d}t}\begin{pmatrix} \frac{\partial b}{\partial X}/\gamma \\ \frac{\partial b}{\partial Y}/\gamma \\ 0 \end{pmatrix}. \tag{2.10}$$

Spatial derivatives may be transformed using the chain rule, which dictates that $\nabla = A^\mathsf{T}\nabla_{\boldsymbol{X}}$, where $\nabla_{\boldsymbol{X}} \equiv (\partial/\partial X, \partial/\partial Y, \partial/\partial Z)^\mathsf{T}$ is the slope-aligned gradient operator.

The governing equations written with respect to this frame, may then be determined to be

$$\frac{\partial \rho}{\partial t} + \dot{\boldsymbol{X}} \cdot \nabla_{\boldsymbol{X}}\rho + \frac{1}{J}\nabla_{\boldsymbol{X}} \cdot (J\rho\boldsymbol{U}) = 0, \tag{2.11a}$$

$$\frac{\partial \psi}{\partial t} + \dot{\boldsymbol{X}} \cdot \nabla_{\boldsymbol{X}}\psi + \frac{1}{J}\nabla_{\boldsymbol{X}} \cdot (J\psi\boldsymbol{U}_s) = 0, \tag{2.11b}$$

$$\rho\left[\frac{\partial \boldsymbol{U}}{\partial t} + \dot{\boldsymbol{X}} \cdot \nabla_{\boldsymbol{X}}\boldsymbol{U} + \boldsymbol{U} \cdot \nabla_{\boldsymbol{X}}\boldsymbol{U}\right] + AA^\mathsf{T}\nabla_{\boldsymbol{X}}p - \boldsymbol{S} - \rho A\boldsymbol{g} = \boldsymbol{R}, \tag{2.11c}$$

where $\boldsymbol{S}$ the transformed divergence of the combined interphase momentum transport and stress tensors, and $\boldsymbol{R}$ is a vector containing any terms that depend on time and space derivatives of the coordinate transformation matrices. To specify the components of $\boldsymbol{S}$ and $\boldsymbol{R}$, we adopt an alternative labelling of the spatial directions $(X_1, X_2, X_3) \equiv (X, Y, Z)$ and employ the Einstein summation convention hereafter, writing

$$S_i = A_{jk}A_{lk}\frac{\partial(T - K)_{il}}{\partial X_j}, \tag{2.12a}$$

$$R_i = -\rho A_{ij}\left[\frac{\partial A_{jk}^{-1}}{\partial t} + (\dot{X}_l + U_l)\frac{\partial A_{jk}^{-1}}{\partial X_l}\right]U_k + A_{ij}A_{lk}(T - K)_{mn}\frac{\partial}{\partial X_l}\left(A_{jm}^{-1}A_{nk}\right). \tag{2.12b}$$

The boundary conditions at the bed transform straightforwardly to

$$\rho^+ W^+ = (\rho_b - \rho^+)M \quad \text{and} \quad \psi^+ W_s^+ = (\psi_b - \psi^+)M. \tag{2.13a,b}$$

At the free surface, we note that $F_h(x, y, z, t) = (H - Z)/\gamma$, where $H \equiv H(X(t), Y(t), t)$ is a reparametrisation of h in the surface-fitted coordinates. Therefore, we may transform Eq. (2.7) and evaluate the resulting equation across the interface, to give

$$\frac{\partial H}{\partial t} + \left(\frac{\partial X}{\partial t} + U_H \right) \frac{\partial H}{\partial X} + \left(\frac{\partial Y}{\partial t} + V_H \right) \frac{\partial H}{\partial Y} - W_H = \frac{\partial Z}{\partial t}, \quad \text{at } Z = H, \qquad (2.14)$$

where $\boldsymbol{U}|_{Z=H(X,Y,t)} \equiv (U_H, V_H, W_H)^\mathsf{T}$.

To obtain a shallow-layer model, we consider flow regimes in which the characteristic thickness of the flow $\mathscr{H}$ is far smaller than its characteristic streamwise length scale $\mathscr{L}$. This suggests the ordering parameter $\epsilon = \mathscr{H}/\mathscr{L} \ll 1$. The topography has its own scale. We permit basal gradients of any size, but choose to constrain the topography by insisting that its characteristic radius of curvature is nowhere smaller than $O(\epsilon^{-1})$. Furthermore, we assume that the rate of change in the bed height due to morphodynamics is no greater than the normal velocity scale. These considerations motivate the following variable rescalings:

$$Z \mapsto \epsilon Z, \quad t \mapsto \epsilon^{-\alpha} t, \quad U \mapsto \epsilon^\alpha U, \quad V \mapsto \epsilon^\alpha V, \quad W \mapsto \epsilon^{\alpha+1} W, \quad p \mapsto \epsilon p, \quad T_{ij} \mapsto \epsilon^{2\alpha+1} T_{ij}, \quad (2.15a\text{–}g)$$

$$M \mapsto \epsilon^{\alpha+1} M, \quad \frac{\partial b}{\partial t} \mapsto \epsilon^{\alpha+1} \frac{\partial b}{\partial t}, \quad \frac{\partial^2 b}{\partial t \partial X_k} \mapsto \epsilon^{\alpha+1} \frac{\partial^2 b}{\partial t \partial X_k}, \quad \frac{\partial^2 b}{\partial X_k X_l} \mapsto \epsilon \frac{\partial^2 b}{\partial X_k X_l}, \quad (2.15h\text{–}k)$$

for all $i, j \in \{1, 2, 3\}$ and $k, l \in \{1, 2\}$. We have included a free parameter $\alpha \geq 0$ in these transformations. The choice to rescale time with respect to this scale will later provide a concrete means of justifying the inclusion of hydrostatic pressure gradients, which becomes important when α exceeds zero. We further assume at this stage, that the velocity difference between the fluid and solid phases is negligible along the plane parallel to the bed slope (so $U = U_s$ and $V = V_s$, to leading order). The corresponding velocities in the normal direction must also scale in accordance with the shallowness assumption. Therefore, we make the additional rescalings

$$W_s \mapsto \epsilon^{\alpha+1} W_s \quad \text{and} \quad K_{ij} \mapsto \epsilon^{2\alpha+2} K_{ij}, \qquad (2.15l,m)$$

for all $i, j \in \{1, 2, 3\}$.

The above transformations may be substituted as necessary into Eqs. (2.9a–c) and (2.10) to determine the leading order components of the coordinate change. In particular, we compute $J = \gamma + O(\epsilon^2)$ and

$$G \equiv AA^\mathsf{T} = \begin{pmatrix} 1 - \frac{1}{\gamma^2} \left[\frac{\partial b}{\partial X} \right]^2 & -\frac{1}{\gamma^2} \frac{\partial b}{\partial X} \frac{\partial b}{\partial Y} & 0 \\ -\frac{1}{\gamma^2} \frac{\partial b}{\partial X} \frac{\partial b}{\partial Y} & 1 - \frac{1}{\gamma^2} \left[\frac{\partial b}{\partial Y} \right]^2 & 0 \\ 0 & 0 & 1 \end{pmatrix} + O(\epsilon^2), \quad \dot{\boldsymbol{X}} = -\frac{\epsilon^{\alpha+1}}{\gamma^2} \frac{\partial b}{\partial t} \begin{pmatrix} \frac{\partial b}{\partial X} \\ \frac{\partial b}{\partial Y} \\ \gamma \end{pmatrix} + O(\epsilon^{\alpha+2}).$$
$$(2.16a,b)$$

Using these expressions, we proceed to apply our variable rescalings to the governing equations (2.11a–c). After simplifying and neglecting any subdominant terms, we obtain

$$\frac{\partial \rho}{\partial t} + M \frac{\partial \rho}{\partial Z} + \frac{\partial}{\partial X}(\rho U) + \frac{\partial}{\partial Y}(\rho V) + \frac{\partial}{\partial Z}(\rho W) = 0, \qquad (2.17a)$$

$$\frac{\partial \psi}{\partial t} + M \frac{\partial \psi}{\partial Z} + \frac{\partial}{\partial X}(\psi U) + \frac{\partial}{\partial Y}(\psi V) + \frac{\partial}{\partial Z}(\psi W_s) = 0, \qquad (2.17b)$$

$$\rho \left[\frac{\partial U}{\partial t} + M \frac{\partial U}{\partial Z} + \boldsymbol{U} \cdot \nabla_{\boldsymbol{X}} U \right] = -\epsilon^{-2\alpha} \frac{\rho g}{\gamma^2} \frac{\partial b}{\partial X} - \epsilon^{1-2\alpha} \left(G_{11} \frac{\partial p}{\partial X} + G_{12} \frac{\partial p}{\partial Y} \right) + \frac{\partial T_{13}}{\partial Z}, \quad (2.17c)$$

$$\rho \left[\frac{\partial V}{\partial t} + M \frac{\partial V}{\partial Z} + \boldsymbol{U} \cdot \nabla_{\boldsymbol{X}} V \right] = -\epsilon^{-2\alpha} \frac{\rho g}{\gamma^2} \frac{\partial b}{\partial Y} - \epsilon^{1-2\alpha} \left(G_{21} \frac{\partial p}{\partial X} + G_{22} \frac{\partial p}{\partial Y} \right) + \frac{\partial T_{23}}{\partial Z}, \quad (2.17d)$$

$$\frac{\partial p}{\partial Z} = -\frac{\rho g}{\gamma} + \epsilon^{2\alpha} \frac{\partial T_{33}}{\partial Z}, \qquad (2.17e)$$

where G_{ij} are the components of the matrix $G = AA^\mathsf{T}$. The corresponding basal boundary conditions [Eqs. (2.13a,b)] are unmodified by the variable transformations, while the constraint on

the free surface becomes

$$\frac{\partial H}{\partial t} + U_H \frac{\partial H}{\partial X} + V_H \frac{\partial H}{\partial Y} - W_H = M. \tag{2.18}$$

We note that these reduced equations contain neither curvature terms nor time derivatives of the basal gradients, since these only appear at higher order. However, these could be reintroduced systematically to obtain a model that includes these effects, as in Refs. [35–37].

Equations (2.17a–e) are to be integrated with respect to the flow depth measured perpendicular to the bed, to obtain depth-averaged flow in two spatial dimensions as depicted earlier, in Fig. 2(d). First, we define the quantities

$$\bar{\rho} = \frac{1}{H} \int_0^H \rho \, dZ, \quad \bar{\psi} = \frac{1}{H} \int_0^H \psi \, dZ, \quad \bar{U} = \frac{1}{H} \int_0^H U \, dZ, \quad \bar{V} = \frac{1}{H} \int_0^H V \, dZ. \tag{2.19a–d}$$

Note that $\bar{\rho}$ and $\bar{\psi}$ are related, via

$$\bar{\rho} = \rho_f + (\rho_s - \rho_f)\bar{\psi}. \tag{2.20}$$

Then, integrating Eqs. (2.17a), (2.17b) and simplifying using the Leibniz rule and the boundary conditions in Eqs. (2.13a,b) and (2.18), gives

$$\frac{\partial}{\partial t}(\bar{\rho}H) + \frac{\partial}{\partial X}(\bar{\rho}H\bar{U}) + \frac{\partial}{\partial Y}(\bar{\rho}H\bar{V}) = \rho_b M, \tag{2.21a}$$

$$\frac{\partial}{\partial t}(\bar{\psi}H) + \frac{\partial}{\partial X}(\bar{\psi}H\bar{U}) + \frac{\partial}{\partial Y}(\bar{\psi}H\bar{V}) = \psi_b M. \tag{2.21b}$$

We have implicitly simplified these equations by omitting terms that arise when averaging over products of the flow variables. For example, in full generality, the second term in Eq. (2.21a) is

$$\frac{\partial}{\partial X} \left[\bar{\rho}H\bar{U} + \int_0^H (\rho - \bar{\rho})(U - \bar{U}) \, dZ \right]. \tag{2.22}$$

However, the common assumption that any slope-normal shear in the velocity profile is negligible permits the simplification of this term and its Y-directed counterpart [46–48]. A similar assumption is used to derive the advective terms in Eq. (2.21b).

Equation (2.17e) may be integrated to obtain hydrostatic pressure, plus a contribution from normal material stresses:

$$p(Z) = \frac{\bar{\rho}g(H - Z)}{\gamma} + \epsilon^{2\alpha}[T_{33}(Z) - T_{33}(H)]. \tag{2.23}$$

Then we compute

$$\int_0^H \frac{\partial p}{\partial X} \, dZ = \frac{\partial}{\partial X} \left(\frac{\bar{\rho}gH^2}{2\gamma} \right) + \epsilon^{2\alpha} \int_0^H \frac{\partial T_{33}}{\partial X} \, dZ. \tag{2.24}$$

A similar formula may be obtained for the depth integral of $\partial p/\partial Y$. We now integrate the momentum equations (2.17c) and (2.17d) over the flow depth, making use of the boundary conditions (2.13a,b), (2.18) and simplifying the pressure gradient terms using Eq. (2.24) and its Y-directed counterpart, ultimately obtaining

$$\frac{\partial}{\partial t}(\bar{\rho}H\bar{U}) + \frac{\partial}{\partial X}(\bar{\rho}H\bar{U}^2) + \frac{\partial}{\partial Y}(\bar{\rho}H\bar{U}\bar{V}) = -\epsilon^{-2\alpha}\frac{\bar{\rho}gH}{\gamma^2}\frac{\partial b}{\partial X}$$
$$-\epsilon^{1-2\alpha}\left(G_{11}\frac{\partial}{\partial X} + G_{12}\frac{\partial}{\partial Y} \right)\left(\frac{\bar{\rho}gH^2}{2\gamma} \right) - T_{13}|_{Z=0^+} + \rho_b U^+ M + \epsilon \int_0^H \frac{\partial T_{33}}{\partial X} \, dZ, \tag{2.25a}$$

$$\frac{\partial}{\partial t}(\bar{\rho}H\bar{V}) + \frac{\partial}{\partial X}(\bar{\rho}H\bar{U}\bar{V}) + \frac{\partial}{\partial Y}(\bar{\rho}H\bar{V}^2) = -\epsilon^{-2\alpha}\frac{\bar{\rho}gH}{\gamma^2}\frac{\partial b}{\partial Y}$$
$$-\epsilon^{1-2\alpha}\left(G_{21}\frac{\partial}{\partial X} + G_{22}\frac{\partial}{\partial Y} \right)\left(\frac{\bar{\rho}gH^2}{2\gamma} \right) - T_{23}|_{Z=0^+} + \rho_b V^+ M + \epsilon \int_0^H \frac{\partial T_{33}}{\partial Y} \, dZ, \tag{2.25b}$$

Note that terms analogous to Eq. (2.22) have been simplified by assuming negligible velocity shear.

The role of the right-hand side forcing terms in Eqs. (2.25a) and (2.25b) depends on the time scale set by α. If $\alpha = 0$ (so that time is not rescaled) then the hydrostatic pressure gradient is subdominant. This occurs when the basal gradients are $O(1)$ and the dynamics are predominantly forced by gravitational acceleration. If instead the gradients are $O(\epsilon)$, then $\alpha = 1$ and the hydrostatic pressure gradient is the same order as gravitational forcing. In order to obtain a model which is appropriate for both steep and gentle topographies, we retain all expressions on the right-hand side which are leading order for any $\alpha \geq 0$. The final terms on the right-hand sides of Eqs. (2.25a,b) are $O(\epsilon)$ and are not retained henceforth. Furthermore, we assume at this stage the the terms containing the basal slip velocities U^+ and V^+ are comparatively small and make implicit the notation that the stress components are to be evaluated at the upper bed surface. On returning to the un-rescaled variables, this leads to the following expressions of momentum balance

$$
\begin{aligned}
\frac{\partial}{\partial t}(\bar{\rho} H \bar{U}) &+ \frac{\partial}{\partial X}\left(\bar{\rho} H \bar{U}^2\right) + \frac{\partial}{\partial Y}(\bar{\rho} H \bar{U} \bar{V}) \\
&+ \frac{1}{\gamma}\left\{\left[1 + (\partial b/\partial Y)^2\right]\frac{\partial}{\partial X} - \frac{\partial b}{\partial X}\frac{\partial b}{\partial Y}\frac{\partial}{\partial Y}\right\}\left(\frac{\bar{\rho} g H^2}{2\gamma^2}\right) = -\frac{\bar{\rho} g H}{\gamma^2}\frac{\partial b}{\partial X} - T_{13},
\end{aligned}
\tag{2.26a}
$$

$$
\begin{aligned}
\frac{\partial}{\partial t}(\bar{\rho} H \bar{V}) &+ \frac{\partial}{\partial X}(\bar{\rho} H \bar{U} \bar{V}) + \frac{\partial}{\partial Y}\left(\bar{\rho} H \bar{V}^2\right) \\
&+ \frac{1}{\gamma}\left\{-\frac{\partial b}{\partial X}\frac{\partial b}{\partial Y}\frac{\partial}{\partial X} + \left[1 + (\partial b/\partial X)^2\right]\frac{\partial}{\partial Y}\right\}\left(\frac{\bar{\rho} g H^2}{2\gamma^2}\right) = -\frac{\bar{\rho} g H}{\gamma^2}\frac{\partial b}{\partial Y} - T_{23}.
\end{aligned}
\tag{2.26b}
$$

The appearance of basal derivatives (via γ) in the hydrostatic pressure and gravitational forcing terms of these equations stems from correctly resolving these forces parallel to the slope. As noted by Iverson & Ouyang [29], these factors are often missing from Earth surface flow models, which can lead to significant errors when steep slopes are present. Furthermore, note that we made use of our assumption of negligible curvature, to rearrange the hydrostatic pressure term and include an additional factor of $1/\gamma$ within the gradient terms. This is necessary to ensure that Eqs. (2.26a) and (2.26b) preserve *lake-at-rest* steady states of the form

$$
\frac{H}{\gamma} + b \equiv \text{const}, \quad \bar{U} = \bar{V} = 0, \quad \bar{\rho} \equiv \text{const},
\tag{2.27}
$$

which correspond to motionless flows with a horizontal free surface. We assume such states to be drag free and non-morphodynamic. (Purely granular flows are not generally expected to achieve this state for example, since they may arrest in non-flat, slumped configurations, due to static basal friction, see e.g. Ref. [49].) After substituting, it may be easily verified that Eq. (2.27) is a solution to Eqs. (2.26a) and (2.26b). Even so, it is nontrivial to design a numerical scheme that preserves these steady states at finite resolution. We show how to do so for our model equations in Sec. 3.

Equations (2.21a,b) and (2.26a,b), plus the bed evolution equation (2.5), comprise a complete set of shallow-layer governing equations for the flow. Returning to the coordinate transformation in Eq. (2.8), we see that after depth-averaging, the surface-fitted coordinates collapse to a Cartesian description where $x \equiv X$ and $y \equiv Y$. Denoting the depth-averaged velocity vector in the Cartesian basis $\{e_x, e_y, e_z\}$ as $\bar{\boldsymbol{u}} = (\bar{u}, \bar{v}, \bar{w})^{\mathsf{T}}$, it is straightforward to see that $\bar{u} = \bar{U}$ and $\bar{v} = \bar{V}$. The remaining component is given by

$$
\bar{w} = \boldsymbol{e}_z \cdot (\bar{U}\boldsymbol{e}_X + \bar{V}\boldsymbol{e}_Y) = \bar{u}\frac{\partial b}{\partial x} + \bar{v}\frac{\partial b}{\partial y}.
\tag{2.28}
$$

Therefore, for the remainder of the paper, we use Cartesian coordinates, since these are convenient for numerical simulations of Earth-surface flows, which are typically run on digital elevation data parametrised in a gravity-aligned frame. However, the curvilinear transformation above was nevertheless required in order to depth integrate the flow along the surface normal and retain the correct geometrical dependence in the model equations. Furthermore, note that since we need not project H onto the vertical when transforming back to Cartesian, it still carries the correct physical meaning of the flow depth measured along the bed normal.

(a) Regularisation

The characteristics λ_1 and λ_2 of our morphodynamic shallow layer model, restricted to the x and y directions respectively, are

$$\lambda_1 = \bar{u} \pm \gamma^{-3/2}\sqrt{gH(1+b_y^2)}, \bar{u}, \bar{u}, 0 \quad \text{and} \quad \lambda_2 = \bar{v} \pm \gamma^{-3/2}\sqrt{gH(1+b_x^2)}, \bar{v}, \bar{v}, 0, \quad (2.29a,b)$$

where $b_x \equiv \partial b/\partial x$ and $b_y \equiv \partial b/\partial y$. The eigenspace associated with these characteristics is degenerate when either

$$\gamma^{3/2}\bar{u} = \sqrt{gH(1+b_y^2)} \quad \text{or} \quad \gamma^{3/2}\bar{v} = \sqrt{gH(1+b_x^2)}, \quad (2.30a,b)$$

since it may be verified that two of the characteristics are zero and both possess the same eigendirection. This implies that the governing equations are not everywhere hyperbolic and consequently ill posed as an initial value problem [50]. This agrees with the more detailed analysis of Ref. [28], which considers a system that is structurally very similar. Therefore, it is essential to regularise the governing equations to obtain well-posed models. Following Ref. [28], we add the terms

$$\frac{\partial}{\partial x}\left(\nu\bar{\rho}H\frac{\partial\bar{u}}{\partial x}\right) + \frac{\partial}{\partial y}\left(\nu\bar{\rho}H\frac{\partial\bar{u}}{\partial y}\right) \quad \text{and} \quad \frac{\partial}{\partial x}\left(\nu\bar{\rho}H\frac{\partial\bar{v}}{\partial x}\right) + \frac{\partial}{\partial y}\left(\nu\bar{\rho}H\frac{\partial\bar{v}}{\partial y}\right) \quad (2.31)$$

to the right-hand sides of the momentum equations (2.26a) and (2.26b) respectively, which model the diffusion of momentum via turbulent eddies. The free parameter ν controls the magnitude of these terms, which are typically expected to be small, relative to other contributions to the flow momentum, since turbulent dissipation occurs at scales smaller than the flow depth. Consequently, it is likely to have only a minimal effect on global flow dynamics. Nevertheless, its inclusion has the desired effect of damping out unphysical resonances that otherwise occur at short wavelengths when the characteristics coalesce.

An illustration of this regularisation is given in Fig. 3(a), using simulations of the governing equations restricted to one spatial dimension. This shows the evolution of a travelling wave on an initially constant slope, prepared such that its uniform tail lies at the transcritical point where the second and fifth characteristics in Eq. (2.29a) intersect. With no regularisation ($\nu = 0\text{m}^2/\text{s}$), the resulting motion is unstable and leads to extremely rapid spatial oscillations, emanating from the front region, which is not initially in morphodynamic equilibrium and acts as a perturbation to the steady tail. These oscillations have approximately zero wave speed and appear as 'noise' in the plotted profile. Applying a sufficiently high eddy viscosity ($\nu = 0.2\text{m}^2/\text{s}$) stabilises the flow. In principle, it is difficult to constrain ν to a particular constant value, since the amount of turbulence dissipation is *a priori* unknown and depends on the spatiotemporal flow dynamics. However, our choice here is commensurate with the hypothesis that the scale of eddy viscosity should depend on the product of the flow depth with the turbulent shear velocity $u_\star = \sqrt{\tau_b/\bar{\rho}}$, where τ_b denotes the magnitude of basal drag (assuming the model closures and parameter choices of Sec. 4). Since it is not our intention to examine the effect of ν in detail, it suffices to illustrate our results herein.

In Fig. 3(b), we show the effect of changing the length scale of the numerical discretisation Δx on a small patch of the free surface. The left-hand panels show the unregularised solution at $t = 160\text{s}$, for the three resolutions labelled on the right-hand panels, which show the corresponding regularised snapshot. The coarsest results use $\Delta x = 2\text{m}$, which is broadly representative of resolutions used in operational shallow flow simulations [21,24,51]. Here, there is little difference between the regularised and unregularised data, which is nearly completely level. In this case, the length scale of the instability is smaller than Δx, so it cannot be captured by the numerics in either case. Corresponding results are shown at $\Delta x = 0.2\text{m}$ and 0.02m. Refinement introduces short unstable wavelengths into the numerical solutions. In the ill-posed case, finer resolution can only lead to increasingly rapid unstable growth, further polluting the free surface. Conversely, the regularised results eventually converge to a level profile. Though the converged profile does ultimately agree with the ill-posed result at 2m resolution (due to the effects of numerical diffusion), we caution that in the ill-posed case, such results are simply not robust enough to be relied upon for flow prediction.
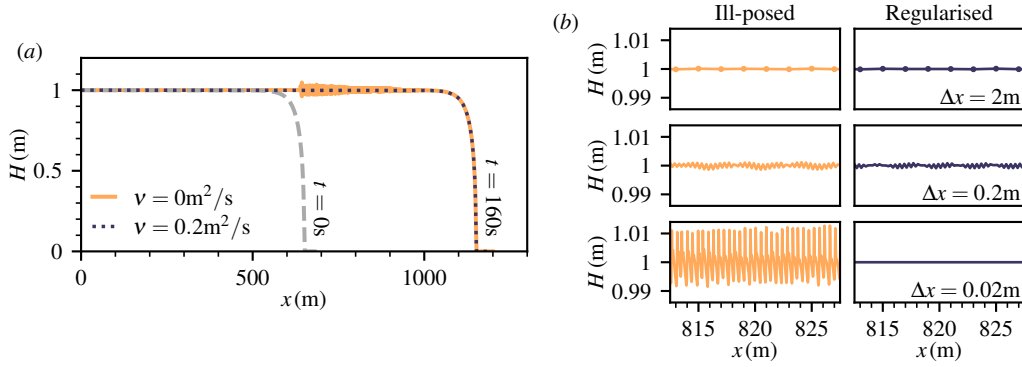
Figure 3. Demonstration of the model regularisation. (*a*) The flow depth as a function of distance, for simulations with $\nu = 0\text{m}^2/\text{s}$ (solid yellow) and $\nu = 0.2\text{m}^2/\text{s}$ (dotted purple) at $t = 160\text{s}$. The grid resolution is $\Delta x = 0.02\text{m}$. The initial condition ($t = 0\text{s}$), plotted in dashed grey, is a steady travelling wave in the governing system without morphodynamics ($M \equiv 0$) on a constant slope, whose gradient (0.04) was selected so that $\bar{u} = \sqrt{gH}/\gamma^{3/2}$ in the uniform tail. The solution was obtained using the numerical method presented in Sec. 3 with the parameters and example closures given in Sec. 4, by numerically integrating flow out from a Dirichlet boundary that imposes $H = 1\text{m}$, $\bar{u} = 3.128\text{m/s}$ (4 s. f.) and $\bar{\psi} = 2.295 \times 10^{-2}$ (4 s. f.) at $x = 0\text{m}$. [The condition on $\bar{u}$ is the velocity of the corresponding steady uniform layer, which may be calculated exactly via Eq. (A 1*a*). The condition on $\bar{\psi}$ is the corresponding solids fraction at which the bed evolution equation possesses a stable equilibrium and may be computed by finding the dilute root of $M(H, \bar{u}, \bar{\psi}) = 0$, given the closures in Eqs. (4.2)–(4.4*b*).] (*b*) Close-up views of the free surface for corresponding simulations with three different grid resolutions, as labelled on the right-hand panels. The left-hand panels use $\nu = 0\text{m}^2/\text{s}$ and the right-hand panels use $\nu = 0.2\text{m}^2/\text{s}$. In the top row only, filled circles show the locations of numerical grid points.

3. Numerical method

In this section, we present an approach for solving the flow equations (2.21*a*,*b*), (2.26*a*,*b*), augmented by the regularising terms (2.31), together with Eq. (2.5) for the bed evolution. Our primary focus is on adapting existing finite volume shallow water schemes to incorporate morphodynamics with a suspended sediment phase and featuring the geometric corrections derived in §2, rather than on constructing a bespoke method.

We firstly write the flow equations in vector form, decomposing them into their hydraulic and morphodynamic components. The mass conservation equations [Eqs. (2.21*a*,*b*)] are linearly recombined to give equations for H and $\bar{\psi}H$. Then we define a vector of primary observables $\boldsymbol{q} \equiv (H, \bar{\psi}H, \bar{\rho}H\bar{u}, \bar{\rho}H\bar{v})^{\mathsf{T}}$, and a two-dimensional gradient operator $\nabla \equiv (\partial/\partial x, \partial/\partial y)^{\mathsf{T}}$. Letting O_n and I_n denote the $n \times n$ zero and identity matrices respectively, the governing system is then given by

$$\frac{\partial \boldsymbol{q}}{\partial t} = \mathcal{H}(\boldsymbol{q}) + \mathcal{M}(\boldsymbol{q}), \tag{3.1a}$$

$$\frac{\partial b}{\partial t} = -\gamma M(\boldsymbol{q}), \tag{3.1b}$$

where

$$\mathcal{H}(\boldsymbol{q}) = -\frac{\partial \boldsymbol{F}_1(\boldsymbol{q})}{\partial x} - \frac{\partial \boldsymbol{F}_2(\boldsymbol{q})}{\partial y} - \gamma B \nabla \zeta(\boldsymbol{q}) + \boldsymbol{S}_1(\boldsymbol{q}) + \boldsymbol{S}_2(\boldsymbol{q}), \tag{3.2a}$$

$$\mathcal{M}(\boldsymbol{q}) = [M(\boldsymbol{q}), \psi_b M(\boldsymbol{q}), 0, 0]^{\mathsf{T}}, \tag{3.2b}$$

with $\zeta = \frac{1}{2}\bar{\rho}gH^2/\gamma^2$,

$$\boldsymbol{F}_1(\boldsymbol{q}) = \left(H\bar{u}, \bar{\psi}H\bar{u}, \bar{\rho}H\bar{u}^2, \bar{\rho}H\bar{u}\bar{v}\right)^{\mathsf{T}}, \quad \boldsymbol{F}_2(\boldsymbol{q}) = \left(H\bar{v}, \bar{\psi}H\bar{v}, \bar{\rho}H\bar{u}\bar{v}, \bar{\rho}H\bar{v}^2\right)^{\mathsf{T}}, \tag{3.3a,b}$$

$$B = \begin{pmatrix} O_2 \\ I_2 - \gamma^{-2}\nabla b \otimes \nabla b \end{pmatrix}, \quad \boldsymbol{S}_1(\boldsymbol{q}) = \left[0, 0, -\frac{\bar{\rho}gH}{\gamma^2}\frac{\partial b}{\partial x} - \tau_{13}(\boldsymbol{q}), -\frac{\bar{\rho}gH}{\gamma^2}\frac{\partial b}{\partial y} - \tau_{23}(\boldsymbol{q})\right]^{\mathsf{T}}, \tag{3.3c,d}$$

$$\boldsymbol{S}_2(\boldsymbol{q}) = [0, 0, \nabla\cdot(\nu\bar{\rho}H\nabla\bar{u}), \nabla\cdot(\nu\bar{\rho}H\nabla\bar{v})]^{\mathsf{T}}. \tag{3.3e}$$

The vector $\boldsymbol{q}$ is discretised spatially over a regular Cartesian mesh by averaging its components over rectangular cells, $c_{i,j} \equiv [x_{i-1/2}, x_{i+1/2}] \times [y_{j-1/2}, y_{j+1/2}]$, defining

$$\boldsymbol{q}_{i,j}(t) = \frac{1}{\Delta x \Delta y}\int_{c_{i,j}}\boldsymbol{q}(x, y, t)\,\mathrm{d}x\,\mathrm{d}y, \quad \text{for } i, j \in \mathbb{Z}, \tag{3.4}$$

where Δx and Δy are fixed grid spacings such that $x_{i+1/2} - x_{i-1/2} = \Delta x$ and $y_{j+1/2} - y_{j-1/2} = \Delta y$. We denote the centroid of $c_{i,j}$ by (x_i, y_j). The full numerical solution vector $\widetilde{\boldsymbol{q}}$ (at each time t) is the collection of all the $\boldsymbol{q}_{i,j}$ for each cell in the simulation domain. The temporal evolution of the numerical problem obeys a system of ordinary differential equations (ODEs) encapsulated by

$$\frac{\mathrm{d}\widetilde{\boldsymbol{q}}}{\mathrm{d}t} = \widetilde{\mathcal{H}}(\widetilde{\boldsymbol{q}}) + \widetilde{\mathcal{M}}(\widetilde{\boldsymbol{q}}), \tag{3.5}$$

where $\widetilde{\mathcal{H}}$ and $\widetilde{\mathcal{M}}$ are suitably chosen discrete approximations to the partial differential operators $\mathcal{H}$ and $\mathcal{M}$ respectively. In particular, $\widetilde{\mathcal{H}}$ is responsible for numerically evaluating the spatial derivatives present in the flux, gradient and diffusive terms of Eq. (3.2a).

Likewise, the bed equation may be spatially discretised by evaluating Eq. (3.1b) over a lattice of points. It is coupled to Eq. (3.5) because the morphodynamics closure M depends on $\boldsymbol{q}$. A convenient way to incorporate this coupling within an existing shallow layer finite volume method is to employ operator splitting to integrate Eq. (3.5). This enables the morphodynamics to be time stepped separately from the flow, leaving the original scheme unmodified. Moreover, we find that this approach simplifies the job of ensuring desirable properties such as mass conservation and steady state preservation, to be discussed shortly. Operator splitting has also been employed recently by Chertock *et al.* for simulating the related (but inequivalent) physical problem of shallow water flows coupled with bed load transport [44].

We propose that the governing equations are evolved in time using the commonplace second-order splitting due to Strang [52], which updates the gridded solution data via the following decomposition

$$\widetilde{\boldsymbol{q}}(t + \Delta t) = \widetilde{\mathcal{H}}_{\Delta t/2}\widetilde{\mathcal{M}}_{\Delta t}\widetilde{\mathcal{H}}_{\Delta t/2}\left[\widetilde{\boldsymbol{q}}(t)\right]. \tag{3.6}$$

Here, $\widetilde{\mathcal{H}}_{\Delta t}$ and $\widetilde{\mathcal{M}}_{\Delta t}$ represent time-discretised analogues of $\widetilde{\mathcal{H}}$ and $\widetilde{\mathcal{M}}$, which approximate the evolution of the respective subproblems

$$\frac{\mathrm{d}\widetilde{\boldsymbol{q}}}{\mathrm{d}t} = \widetilde{\mathcal{H}}(\widetilde{\boldsymbol{q}}), \quad \frac{\mathrm{d}\widetilde{\boldsymbol{q}}}{\mathrm{d}t} = \widetilde{\mathcal{M}}(\widetilde{\boldsymbol{q}}), \tag{3.7a,b}$$

over an interval Δt forward in time using appropriately chosen time stepping algorithms. This approach effectively decouples the hydraulic and morphodynamic physics from a numerical point of view. The bed equation need only be solved in concert with the morphodynamic part, while the implementation of the hydraulic operator may assume that the bed surface is static. Therefore, we split the remainder of this section into separate discussions of the hydraulic and morphodynamic numerics.

(a) Hydraulic step

The hydraulic component of our governing equations involves mostly standard, or slightly modified versions of terms found in classical shallow water formulations. Consequently, the

evaluation of $\widetilde{\mathcal{H}}_{\Delta t}$ may be achieved by extending existing schemes that are well documented elsewhere [53–55]. We base our particular implementation on the central-upwind finite volume solver of Chertock *et al*. [56], which possesses desirable qualities, including the exact preservation of steady states (including lake-at-rest) and guaranteed positivity of the flow depth. Since the full details of this method are not our focus, we concentrate only on describing the specific adaptations that are needed to solve our model. We have endeavoured to keep our framing as general as possible, so that these adaptations can be used to augment other shallow water schemes.

At any point in the simulation, each of the flux terms within $\widetilde{\mathcal{H}}$ may be evaluated on $\widetilde{\boldsymbol{q}}$ at (x_i, y_j), using numerical derivatives of the form

$$\frac{\partial f}{\partial x}(x_i, y_j) \approx \frac{f(\boldsymbol{q}_{i+1/2,j}) - f(\boldsymbol{q}_{i-1/2,j})}{\Delta x}, \quad \frac{\partial f}{\partial y}(x_i, y_j) \approx \frac{f(\boldsymbol{q}_{i,j+1/2}) - f(\boldsymbol{q}_{i,j-1/2})}{\Delta y}, \quad (3.8a,b)$$

where f is a field in $\boldsymbol{F}_1$ or $\boldsymbol{F}_2$ respectively. Here, we abuse notation slightly: $f(\boldsymbol{q}_{i\pm1/2,j})$ and $f(\boldsymbol{q}_{i,j\pm1/2})$ should be understood as numerical fluxes, i.e. approximations to the average value of f evaluated across the cell interfaces $\{x_{i\pm1/2}\} \times [y_{j-1/2}, y_{j+1/2}]$ and $[x_{i-1/2}, x_{i+1/2}] \times \{y_{j\pm1/2}\}$ respectively. Various strategies exist for the computation of numerical fluxes, the details of which are fairly complicated and not especially important here. Unfamiliar readers may refer to e.g. Ref. [53] for an overview. The diffusive terms in $\boldsymbol{S}_2$ may be computed within the framework of numerical fluxes, or via finite difference stencils, as in Ref. [57] for example. In our implementation, to compute the first term of diffusion in the x-direction, we employ a variation on an approach documented by Kurganov and Tadmor [58], setting $f = \nu \bar{\rho} H \partial \bar{u}/\partial x$ and computing the corresponding numerical flux as the average of two approximate values either side of the relevant interface via the general formula:

$$f(\boldsymbol{q}_{i+1/2,j}) = \frac{1}{2}\left[f\left(\boldsymbol{q}_{i+1/2,j}^-, (\boldsymbol{q}_x)_{i,j}\right) + f\left(\boldsymbol{q}_{i+1/2,j}^+, (\boldsymbol{q}_x)_{i+1,j}\right)\right]. \quad (3.9)$$

Here, $\boldsymbol{q}_{i+1/2,j}^- = \boldsymbol{q}_{i,j} + \Delta x(\boldsymbol{q}_x)_{i,j}/2$, $\boldsymbol{q}_{i+1/2,j}^+ = \boldsymbol{q}_{i+1,j} - \Delta x(\boldsymbol{q}_x)_{i+1,j}/2$, are reconstructions of $\widetilde{\boldsymbol{q}}$ at either side of the corresponding cell interface, using $(\boldsymbol{q}_x)_{i,j}$ and $(\boldsymbol{q}_x)_{i+1,j}$, which denote numerical approximations to $\partial \boldsymbol{q}/\partial x$ at (x_i, y_j) and (x_{i+1}, y_j) respectively. These latter terms are routinely computed as part of central-upwinding schemes (separate from, but in conjunction with the flux derivatives themselves) by using flux-limiting formulae. Computation of $\bar{\rho}_{i,j}$, which is required, but not explicitly available in $\boldsymbol{q}_{i,j}$ is discussed shortly. Analogous formulae to Eq. (3.9) may be applied to compute the remaining components of the Laplacian.

In the case of evaluating the hydrostatic pressure term, $\gamma B \nabla \zeta$, particular attention must be paid to the problem of preserving lake-at-rest solutions, defined above in Eq. (2.27) to be stationary states with a horizontal free surface. Schemes that do not compute these states exactly generate spurious momentum from static initial conditions. This is undesirable for simulations of Earth surface flows that can naturally arrest. It is easily verified from the governing equations that numerically preserving these states requires that in the resting configuration [Eq. (2.27)], the discretised hydrostatic pressure gradient and gravitational forcing exactly balance. Recall that we do not include rheologies that exert nonzero basal stresses when resting in these considerations, since they may adopt a non-horizontal free surface when at rest.

To achieve this, we make use of a second-order discretisation due to Kurganov and Levy [54] that computes these terms using values for the flow surface $\eta \equiv H/\gamma + b$ at cell centres and the bed height b at cell vertices. Consequently, we store and update b at the cell vertices $(x_{i\pm1/2}, y_{j\pm1/2})$ and use linear interpolation to obtain the necessary topographic data at cell interfaces

$$b_{i\pm1/2,j} = \frac{1}{2}\left(b_{i\pm1/2,j-1/2} + b_{i\pm1/2,j+1/2}\right), \; b_{i,j\pm1/2} = \frac{1}{2}\left(b_{i-1/2,j\pm2} + b_{i+1/2,j\pm2}\right) \quad (3.10a,b)$$

and centres

$$b_{i,j} = \frac{1}{2}\left(b_{i-1/2,j} + b_{i+1/2,j}\right), \; (b_x)_{i,j} = \frac{b_{i+1/2,j} - b_{i-1/2,j}}{\Delta x}, \; (b_y)_{i,j} = \frac{b_{i,j+1/2} - b_{i,j-1/2}}{\Delta y}. \quad (3.11a\text{–}c)$$

Then, for the hydrostatic pressure gradient, we write $\zeta = \frac{1}{2}\bar{\rho}g(\eta - b)^2$ and compute

$$\gamma(x_i, y_j) B(x_i, y_j) \left[\frac{\partial \zeta}{\partial x}(x_i, y_j), \frac{\partial \zeta}{\partial y}(x_i, y_j) \right]^{\mathsf{T}}, \tag{3.12}$$

evaluating the geometric terms γ, B at cell centres, using Eqs. (3.10*a,b*) and (3.11*a–c*) with their respective formulae in Eqs. (2.4) and (3.3*c*), and evaluating the ζ derivatives via suitable numerical fluxes as per the discussion around Eqs. (3.8*a,b*). The gravitational forcing term is similarly evaluated at each cell centre. Its discretisation, by way of Eqs. (3.11*a–c*), is

$$-\frac{\bar{\rho}_{i,j} g(\eta_{i,j} - b_{i,j})}{\gamma(x_i, y_j)} \left[(b_x)_{i,j}, (b_y)_{i,j} \right]^{\mathsf{T}}. \tag{3.13}$$

In both Eqs. (3.12) and (3.13), $\bar{\rho}_{i,j}$ must be determined from $\boldsymbol{q}_{i,j}$. It may be computed via Eq. (2.20), after obtaining $\bar{\psi}_{i,j}$ from $(\bar{\psi}H)_{i,j}$, by using an appropriate formula that guards against numerical singularities when flow depths are small [56], such as

$$\bar{\psi}_{i,j} = \frac{2H_{i,j}(\bar{\psi}H)_{i,j}}{H_{i,j}^2 + \max\{H_{i,j}^2, H_\epsilon^2\}}, \tag{3.14}$$

where H_ϵ is a small constant. In our implementation, we use $H_\epsilon = 10^{-6}$ m. Analogous formulae may deployed (when required) to obtain the flow velocity from $(\bar{\rho}H\bar{u})_{i,j}$ and $(\bar{\rho}H\bar{v})_{i,j}$.

It may now be verified that the numerical terms in Eqs. (3.12) and (3.13) exactly balance for lake-at-rest flows. The presence of the matrix B [defined in Eq. (3.3*c*)] makes confirming this fact slightly more complicated than in prior instances of schemes for the classical shallow water equations [45,54,56]. We show it explicitly in Appendix A.

The remaining terms in $\widetilde{\mathcal{H}}$ yet to be discussed are the cell-averaged components of the bottom drag closures, $\tau_{13}(\boldsymbol{q})$ and $\tau_{23}(\boldsymbol{q})$. Regardless of the choice of model parametrisation, these should not be evaluated naively on $\boldsymbol{q}_{i,j}$, which only contains the horizontal components of momentum. For simplicity, assume that the drag force density vector depends isotropically on the flow velocity, i.e. it has magnitude $\tau_b \equiv \tau_b(|\bar{\boldsymbol{u}}|; H, \bar{\psi})$. Then, at each cell $c_{i,j}$, we must evaluate

$$(\tau_{13}, \tau_{23})_{i,j} = \tau_b(|\bar{\boldsymbol{u}}_{i,j}|) \frac{(\bar{u}_{i,j}, \bar{v}_{i,j})}{|\bar{\boldsymbol{u}}_{i,j}|}, \quad \text{where } |\bar{\boldsymbol{u}}_{i,j}| = \sqrt{\bar{u}_{i,j}^2 + \bar{v}_{i,j}^2 + \left(\bar{u}_{i,j}(b_x)_{i,j} + \bar{v}_{i,j}(b_y)_{i,j} \right)^2}. \tag{3.15}$$

This formula ensures that the contribution of the vertical velocity [Eq. (2.28)] is consistently transmitted to the momentum balance by accounting for the underlying basal geometry.

Furnished with the means to compute the various components of $\widetilde{\mathcal{H}}(\widetilde{\boldsymbol{q}})$, the hydraulic subproblem [Eq. (3.7*a*)] may be time stepped from a given initial condition, using any number of suitable methods. In our implementation, we follow Chertock *et al.* [56] and use a second-order semi-implicit Runge-Kutta scheme, detailed in Ref. [59]. To construct a scheme that is mass conserving, we must be observant of the geometry of the system. The total volume of mixed material and of solids may be obtained by integrating over the flow and recalling that the Jacobian determinant of the transformation to slope-fitted coordinates is γ (up to order ϵ^2). These are given by

$$\int_{\mathbb{R}^2} H\gamma \, \mathrm{d}x \, \mathrm{d}y \quad \text{and} \quad \int_{\mathbb{R}^2} \bar{\psi}H\gamma \, \mathrm{d}x \, \mathrm{d}y, \tag{3.16}$$

respectively. Expressions for the total mass of fluids and solids are linearly dependent on these integrals. Therefore, to conserve these quantities during the hydraulic step, it is sufficient to conserve the fluxes of $H\gamma$ and $\bar{\psi}H\gamma$ across numerical cells. This is achieved by updating $H_{i,j}$ over the time interval Δt as so

$$H_{i,j}(t + \Delta t) - H_{i,j}(t) =$$
$$-\frac{\Delta t}{\gamma_{i,j}} \left\{ \left[\frac{(H\bar{u}\gamma)_{i+1/2,j}}{\Delta x} - \frac{(H\bar{u}\gamma)_{i-1/2,j}}{\Delta x} \right] + \left[\frac{(H\bar{v}\gamma)_{i,j+1/2}}{\Delta y} - \frac{(H\bar{v}\gamma)_{i,j-1/2}}{\Delta y} \right] \right\}, \tag{3.17}$$

where $\gamma_{i,j} = \gamma(x_i, y_j)$. The numerical fluxes on the right-hand side of Eq. (3.17) should be understood as being evaluated via an appropriate method, as indicated in the discussion around Eq. (3.8a,b). Regardless of how they are approximated, the sum of these fluxes over the whole simulation domain is zero, so $H\gamma$ is conserved between time steps. An analogous formula may be used to update $(\bar{\psi}H)_{i,j}$.

In order to evolve $\eta = H/\gamma + b$, we take advantage of the fact that within the hydraulic operator, $\partial\eta/\partial t = \gamma^{-1}\partial H/\partial t$. Therefore, we may integrate each $\eta_{i,j}$ using the update to $H_{i,j}$, i.e.

$$\eta_{i,j}(t + \Delta t) = \eta_{i,j}(t) + \gamma_{i,j}^{-1}\left[H_{i,j}(t + \Delta t) - H_{i,j}(t)\right]. \tag{3.18}$$

It is not strictly necessary to explicitly store $H_{i,j}$ in order to apply this formula. The steps in Eqs. (3.17) and (3.18) may be combined to time step the hydraulic subproblem conservatively. Schemes which make the small angle approximation $\gamma = 1$ may fail to be truly mass conservative if they solve equations which conserve the flow depth measured along the vertical.

(b) Morphodynamic step

In the morphodynamic step, we first time step b. Since the topographic data is discretised at cell vertices, we interpolate $\widetilde{\boldsymbol{q}}$, computing

$$\boldsymbol{q}_{i+1/2, j+1/2} = \frac{1}{4}\left(\boldsymbol{q}_{i,j} + \boldsymbol{q}_{i+1,j} + \boldsymbol{q}_{i,j+1} + \boldsymbol{q}_{i+1,j+1}\right) \tag{3.19}$$

for each vertex point $(x_{i+1/2}, y_{j+1/2})$. The bed may then be evolved by time stepping the ODEs

$$\frac{\mathrm{d}b_{i+1/2, j+1/2}}{\mathrm{d}t} = -\gamma_{i+1/2, j+1/2}M\left(\boldsymbol{q}_{i+1/2, j+1/2}\right). \tag{3.20}$$

We compute the corresponding morphodynamic updates to the flow variables by determining them directly from the changes in bed height over the time interval Δt (which, in the case of an explicit multi-step method should be understood as the increment of a particular substep).

Conservation of mass requires that the total amount of material eroded from (or deposited to) the bed is added to (or subtracted from) the flow. Across cell $c_{i,j}$, this has volume

$$\frac{\Delta x \Delta y}{4}\sum_{\hat{v} \in \hat{V}(c_{i,j})} \Delta b_{\hat{v}} = \Delta x \Delta y \Delta b_{i,j}, \tag{3.21}$$

where $\hat{V}(c_{i,j})$ denotes the set of $c_{i,j}$'s four vertices and $\Delta b_{\hat{v}}$, $\Delta b_{i,j}$ are the changes in b over the time interval Δt, at the vertex $\hat{v}$ and cell $c_{i,j}$ respectively. To ensure that the update is conservative, we can insist that this is equal and opposite to the corresponding change to flow volume $H_{i,j}\gamma_{i,j}$, over $c_{i,j}$. In other words, we require

$$\Delta b_{i,j} = -\left[(H\gamma)_{i,j}(t + \Delta t) - (H\gamma)_{i,j}(t)\right]. \tag{3.22}$$

After rearranging for $(H\gamma)_{i,j}(t + \Delta t)$, this implies that η may be time stepped according to

$$\eta_{i,j}(t + \Delta t) = \frac{1}{\gamma_{i,j}(t + \Delta t)^2}\left[(H\gamma)_{i,j}(t) - \Delta b_{i,j}\right] + b_{i,j}(t + \Delta t). \tag{3.23}$$

Similarly, since we assume that the bed consists of saturated solids occupying volume fraction ψ_b, the solids fraction of each cell may be updated by

$$(\bar{\psi}H)_{i,j}(t + \Delta t) = \frac{1}{\gamma_{i,j}(t + \Delta t)}\left[(\bar{\psi}H\gamma)_{i,j}(t) - \psi_b\Delta b_{i,j}\right]. \tag{3.24}$$

The steps above are sufficient to time step the morphodynamic subproblem in Eq. (3.7b), which completes the numerical scheme in principle. However, there are various issues to be mindful of when implementing the scheme in an operational code that are particular to morphodynamic flows.

(c) Practical considerations

In operational debris flow simulations, where flows travel over great distances (tens of kilometres) it is often practically necessary to limit the grid resolution to achieve feasible computation times. Therefore, we recommend applying some consistency checks during the numerics.

The time step taken for the hydraulic subproblem should be adaptively limited by the standard Courant-Friedrichs-Lewy (CFL) condition, which prevents information from travelling farther than a fixed fraction of the grid spacing [53,56]. The system characteristics given in Eq. (2.29) (which differ from those of classical shallow water equations) are used for this calculation. On very fine grids, the diffusive time scale $\min\{\Delta x^2/\nu, \Delta y^2/\nu\}$ may be comparable to the hydraulic time step given by the CFL condition. It is necessary for stability to limit the time step to the smaller of the two. We suggest further verifying *a posteriori* that between morphodynamic steps

$$|H_{i,j}(t + \Delta t) - H_{i,j}(t)| < \beta H_{i,j}(t), \tag{3.25}$$

for all $c_{i,j}$ and some fixed $\beta < 1$, so that the relative change in flow depth is not too great. If this condition is violated, Δt may be refined and the time step recomputed. Note that since the time step is shared between the two subproblems in the splitting scheme [Eq. (3.6)], the prior hydraulic step must also be recomputed in this case. We have used $\beta = 0.1$ to compute the results herein.

Even if a very small time step is taken, it is possible when calculating $\Delta b_{i,j}$, for a cell to deposit a larger volume of solids that it possesses according to the value of $\bar{\psi}_{i,j}$. The volume of flow that is available to be deposited within a cell occupies a fraction $\bar{\psi}_{i,j}/\psi_b$ of the volume. Therefore 'excess' deposition occurs at $c_{i,j}$ if

$$\Delta b_{i,j} > \frac{(\bar{\psi} H \gamma)_{i,j}(t)}{\psi_b}, \tag{3.26}$$

which we can see from Eq. (3.24) would leave $(\bar{\psi} H)_{i,j}$ negative. As well as being unphysical, such a step can be disastrous for the solver if it ultimately leads to the computation of negative flow depths. Nevertheless, it is not always practical to refine Δt and recompute the morphodynamic step until no cell satisfies inequality (3.26). Therefore, we opt to apply a correction to these cells. Making such an adjustment is complicated by the fact that $\Delta b_{i,j}$ is contingent on all four of the bed updates at $c_{i,j}$'s vertices, in accordance with Eqs. (3.10a,b) and (3.11a). Each vertex $\hat{v} \in \hat{V}(c_{i,j})$ may be 'depositional' or 'erosive' over Δt, depending on the sign of $\Delta b_{\hat{v}}$. In order for inequality (3.26) to be satisfied, at least one of them must have $\Delta b_{\hat{v}} > 0$. We denote by $\hat{V}_D(c_{i,j}; t, \Delta t)$, the set of vertices where the bed update at time t is positive and correct only these vertices. Specifically, for each $\hat{v} \in \hat{V}_D(c_{i,j}; t, \Delta t)$ we adjust the the bed height update from $\Delta b_{\hat{v}}$ to $\Delta b_{\hat{v}}(1 - \delta_{\hat{v}})$, where (omitting time dependence)

$$\delta_{\hat{v}} = \frac{4\left[\Delta b_{i,j} - (\bar{\psi} H \gamma)_{i,j}/\psi_b\right]}{\sum_{\hat{v} \in \hat{V}_D(c_{i,j})} \Delta b_{\hat{v}}}. \tag{3.27}$$

Note that $\delta_{\hat{v}} > 0$, due to inequality (3.26). Moreover, by consulting Eqs. (3.10a,b) and Eq. (3.11a), we see that

$$4\Delta b_{i,j} = \sum_{\hat{v} \in \hat{V}(c_{i,j})} \Delta b_{\hat{v}} \leq \sum_{\hat{v} \in \hat{V}_D(c_{i,j})} \Delta b_{\hat{v}}. \tag{3.28}$$

and conclude $\delta_{\hat{v}} \leq 1$. Since $\delta_{\hat{v}} \in (0, 1]$, the corrected bed update at each vertex is always smaller (less depositional), but preserves its original sign (it never becomes erosional). After updating the vertices, the flow variables η and $\bar{\psi} H$ must be recomputed, via Eqs. (3.23) and (3.24), for all cells $c_{k,l}$ such that $\hat{V}(c_{k,l}) \cap \hat{V}_D(c_{i,j}) \neq \emptyset$. Finally, we note that there may be neighbouring cells that satisfy inequality (3.26). In this case, a vertex may receive up to four corrections. Therefore, as successive updates are applied, Eq. (3.27) must be computed from the numerical solution that incorporates any updates already proposed for neighbouring cells. This ensures that vertices which receive multiple corrections are not 'over-corrected'—i.e. the cumulative effect of multiple updates may still be encapsulated as $\Delta b_{\hat{v}} \mapsto (1 - \delta)\Delta b_{\hat{v}}$ for some $\delta \in (0, 1]$.

We suggest only applying this correction procedure to cells whose flow depths are very low, so that any adjustments made are small compared with the total flow volume. For our results

Table 1. Parameter values used in the example simulations.

C_d	ψ_b	ε	d (m)	g (m/s^2)	ρ_f (kg/m^3)	ρ_s (kg/m^3)	w_s (m/s)
0.04	0.65	2.5×10^{-3}	5×10^{-3}	9.81	1000	2000	0.2

in the next section, we make the correction on any cell satisfying both inequality (3.26) and $H_{i,j} < H_\epsilon = 10^{-6}$m. If a deeper cell is found to satisfy inequality (3.26), then we refine the time step and recompute it.

4. Example solutions

In order to demonstrate the scheme in operation, we present some results on two simple initial topographies: a uniform slope and a surface that smoothly transitions between two constant grades. While our governing equations and numerical methods are applicable for a wide range of closures, spanning both granular and fluid-like flows, we employ simple expressions for our illustrative results. For τ_b, we use a turbulent fluid (or Chézy) drag closure:

$$\tau_b(|\bar{\boldsymbol{u}}|) = \bar{\rho} C_d |\bar{\boldsymbol{u}}|^2,$$ (4.1)

where C_d is a positive coefficient. This is physically appropriate for flows with low solids content and analytically convenient, due to its relative simplicity.

The morphodynamic transfer term may be thought of as a competition between rates of erosion $E \geq 0$ and deposition $D \geq 0$, exchanging saturated granular material at the basal solids fraction ψ_b. The magnitudes of E and D depend on the local flow conditions. We write this as

$$M(H, \bar{\boldsymbol{u}}, \bar{\psi}) = \chi(H) \left[\frac{E(\bar{\boldsymbol{u}}) - D(\bar{\psi})}{\psi_b} \right].$$ (4.2)

The function χ is included in order to damp morphodynamics out when the flow is very shallow. We find this to be a practical necessity that prevents the unphysical bulking of rapid, thin flows. Therefore, we set

$$\chi(H) = \frac{1}{2} \left\{ 1 + \tanh \left[a \log \left(\frac{H}{H_c} \right) \right] \right\},$$ (4.3)

where H_c is a characteristic length scale at which morphodynamic processes decay with decreasing flow depth, and a is a free parameter that dictates how sharp the decay is. Note that $\lim_{H \to 0} \chi(H) = 0$ and $\chi(H) \approx 1$ when $H \gg H_c$. In all simulations, we set $H_c = d$ and $a = 10$.

Two simple closures that capture the essential physics of erosion and deposition are given by

$$E(|\bar{\boldsymbol{u}}|) = \frac{\varepsilon \tau_b(|\bar{\boldsymbol{u}}|)}{\bar{\rho} u_p} \quad \text{and} \quad D(\bar{\psi}) = w_s \bar{\psi} \left(1 - \frac{\bar{\psi}}{\psi_b} \right).$$ (4.4a,b)

Here, erosion is proportional to the basal friction with non-negative dimensionless coefficient ε, which controls the erodibility of the substrate. This is a simplified analogue of empirical formulae that predict erosion rates according to power laws of dimensionless basal (Shields) stress, beyond an incipient threshold value (taken to be zero here) [60]. The normalising factor $u_p = (g'_\perp d)^{1/2}$ is a characteristic particle velocity, where $g'_\perp = g(\rho_s/\rho_f - 1)/\gamma$ is the reduced gravity resolved normal to the slope and d is the diameter of solid particles. The quadratic deposition function allows for the effects of hindered settling at high solids concentrations. It phenomenologically captures the empirical formulae of Richardson & Zaki [61] and others [62]. The free parameter w_s sets the characteristic settling velocity of particles. We fix illustrative parameter values throughout this section, chosen to be representative of natural materials. These are given in table 1.

In our simulations we use an equispaced numerical grid with $\Delta x = \Delta y$. Each result below was computed at multiple resolutions in order to verify that solution vectors on successively fine grids approach a limiting state as $\Delta x \to 0$. However, since our primary intention is to demonstrate the numerical scheme in operation, we are ultimately only concerned that presented solutions are qualitatively converged, in the sense that any essential flow features that we describe ought
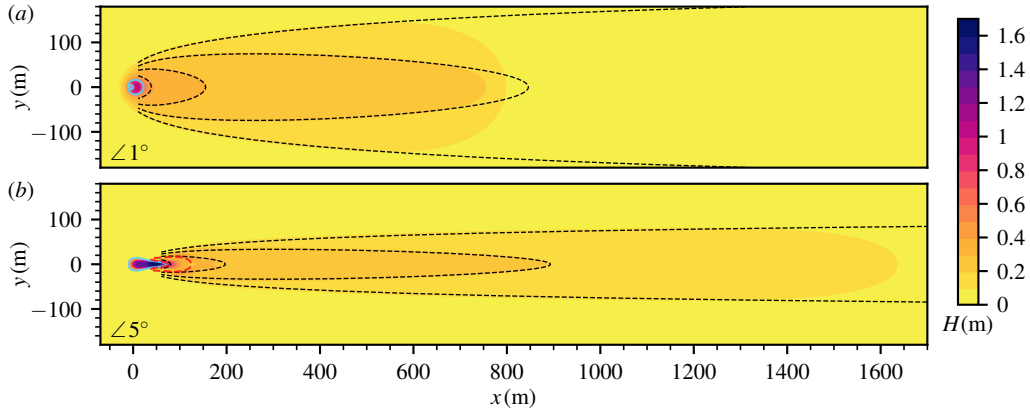
Figure 4. Flows propagating on constant initial slopes of (*a*) $1°$ and (*b*) $5°$ inclination, fed by a $50\mathrm{m}^3/\mathrm{s}$ point source flux at the origin. Filled contours show the flow depth H at $t = 800\mathrm{s}$ at increments of $0.1\mathrm{m}$. Solid blue lines bound regions where the cumulative effect of morphodynamics has eroded the bed by more than $0.1\mathrm{m}$. Likewise, the dashed red line in (*b*) encloses a region within which deposit heights exceed $0.1\mathrm{m}$. (Both these regions are localised near to the source flux.) Dashed black lines show the contours of the corresponding analytical similarity solution, given in Eqs. (4.7*a*–*c*) and (4.8*a*–*c*), at 0.1, 0.2 and $0.3\mathrm{m}$. The grid resolutions are $\Delta x = $ (*a*) $1\mathrm{m}$ and (*b*) $0.5\mathrm{m}$.

to be preserved under grid refinement. For any flow variable f, we denote its corresponding numerical solution on the grid of width Δx, by $f^{\Delta x}(t)$ and restrict our consideration of this vector to its components $f_{i,j}^{\Delta x}(t)$ within the inundated region, whose grid points are indexed by the set $I(t) = \{(i,j) : H_{i,j}^{\Delta x}(t) > H_\epsilon\}$. The discrepancy between two discrete solution fields at different resolutions may be measured by projecting the finer solution onto the coarser grid and computing the normalised residual of their difference (omitting time dependence):

$$R(\Delta x_1, \Delta x_2; f) = \frac{\left|f^{\Delta x_1} - f^{\Delta x_2}\right|_{L^1}}{\left|f^{\Delta x_2}\right|_{L^1}}, \quad \text{where} \quad \left|f^{\Delta x}\right|_{L^1} = \frac{1}{|I|} \sum_{(i,j) \in I} \left|f_{i,j}^{\Delta x}\right|. \tag{4.5}$$

We have verified that $R(\Delta x, \Delta x/2; f) < R(2\Delta x, \Delta x; f)$ and ensured that all the solutions presented satisfy $R(\Delta x, \Delta x/2; f) < R_\epsilon = 0.05$ for all $f \in \{H, H\bar\psi, \bar\rho H\bar u, \bar\rho H\bar v, b - b_0\}$, where b_0 denotes the initial bed height. In other words, halving the grid spacing changes none of the solution variables by more than 5% on average. For most of our results the convergence of each field is closer to 1%. A single exception to this is the $\bar\rho H\bar v$ field of the Fig. 6 result, which was far tougher to resolve due to the presence of a roll wave instability, requiring us to relax the convergence criterion to $R_\epsilon = 0.08$ in this case. The grid discretisation for each result is provided in the corresponding figure caption.

(a) Uniform slopes.

On the following initial slope inclined at angle ϑ,

$$b(x, y, 0) = -\tan(\vartheta)x, \tag{4.6}$$

we simulate flows spreading from a constant dilute source flux $Q = 50\mathrm{m}^3/\mathrm{s}$ at $(x, y) = (0, 0)$. The source is computed by adding $Q\Delta t/(\gamma_{i,j}^2 N_s \Delta x \Delta y)$ to the η time-stepping update in Eq. (3.18), for each cell whose centre lies within a radius of $10\mathrm{m}$ from the origin, where N_s denotes the number of such cells. Provided that the flow travels over a far greater distance than the source radius, this procedure approximates a point source and it is referred to as such below.
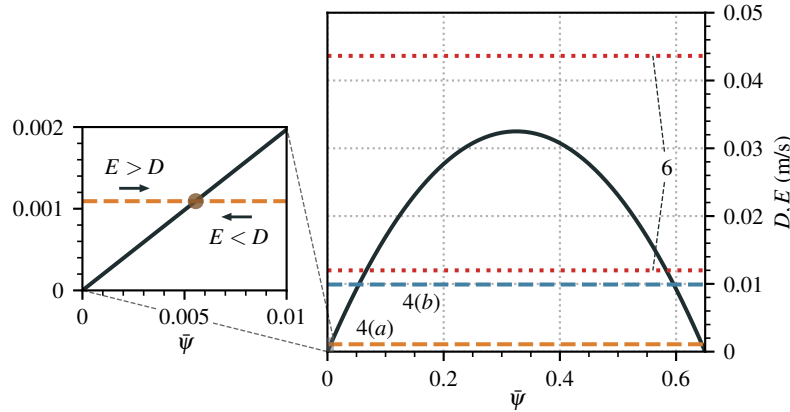
Figure 5. Erosion and deposition rates from the constant slope simulations as a function of flow solid fraction $\bar{\psi}$. The solid black curve is the deposition rate $D(\bar{\psi})$, while the orange and blue dashed curves show erosion rate $E(|\bar{u}_{\max}|)$, where $|\bar{u}_{\max}|$ is the maximum flow speed within the inundated area of the flows presented in Figs. 4(a) and (b), as labelled. The dotted red curves show E for $|\bar{u}| = 9.69\text{m/s}$ and 5.08m/s. These values are the maximum flow speeds (to 3 s. f.) computed for the result given below in Fig. 6, over its two distinct regimes, which we designate as $x < 250\text{m}$ and $x > 250\text{m}$ respectively.

(i) Gentle slopes.

Figure 4 shows contour plots of the flow depth after $t = 800\text{s}$ for two different initial slope angles, (a) $\vartheta = 1°$ and (b) $\vartheta = 5°$. Both results feature significant erosion of the bed: as much as (a) -0.62m and (b) -2.5m respectively. However, this is confined to compact regions near the source. Blue contours bound regions within which the net change in bed height due to erosion is below -0.1m. The $5°$ flow features a region within which net deposition of the excavated bed material exceeds 0.1m, indicated by the dashed red bounding curve. Outside these regions, the down- and cross-slope expansion of the flow is approximately steady and the bed exchange term attains a dynamic balance. Indeed, across the extent of the flow that is inundated up to a depth of 0.1m and more than 200m from the source, we compute $\max(|E - D|/E) \le$ (a) 6×10^{-3} and (b) 0.04.

The equilibration of erosion and deposition occurs because, for each speed $|\bar{u}|$ present in the flow, there exists a stable sediment concentration that the system relaxes onto at each point. The essential mechanism for this was explored previously in Ref. [28]. We illustrate it graphically in Fig. 5. This shows the deposition rate curve and example erosion rate curves, each as a function of $\bar{\psi}$. For both the $1°$ and $5°$ flows, these intersect at two locations where D and E are exactly balanced. As highlighted in the enlarged portion of Fig. 5, perturbations away from the more dilute intersection point induce negative feedback from the morphodynamics that acts to return the system to equilibrium. While the flow speed (and hence the erosion rate) varies spatially throughout each flow, it nowhere reaches a value that would cause E to exceed the maximum deposition rate, $D(\psi_b/2)$. Therefore, at each inundated point in these solutions, a stable equilibrium exists and we have verified from the data that these equilibria are approximately attained outside the vicinity of the source flux region.

Since these flows are approximately steady with almost vanishing morphodynamics downstream from the source, it is possible to construct analytical solutions by hypothesising that these properties become asymptotically exact at long times. In Appendix B, we show how to derive these for a general class of drag closures. When specialised to the current case of Chézy drag, we recover the following solutions, with a form previously obtained by Bonnecaze & Lister [63]:

$$H(x,\xi) = C_H x^{-1/4}(1 - \xi^2), \quad w_p(x) = C_w x^{3/8}, \quad \bar{u}(x,\xi) = \Lambda H^{1/2}, \quad (4.7a\text{–}c)$$
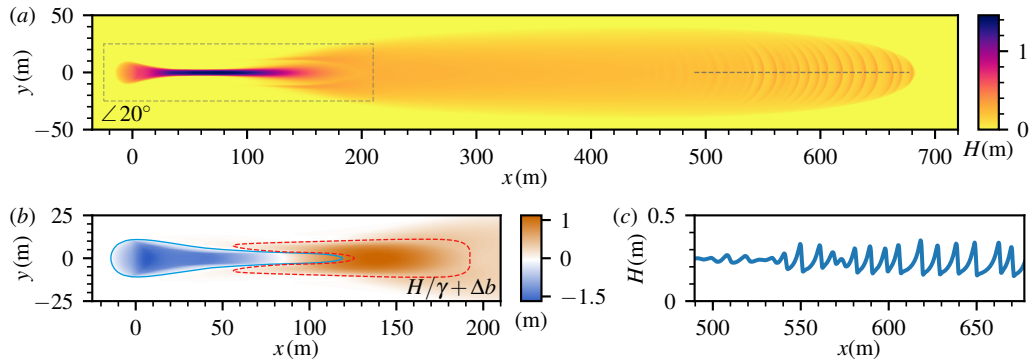
Figure 6. Flow propagating on an incline with a constant initial slope of $20°$, fed by a $50\mathrm{m}^3/\mathrm{s}$ point source flux at the origin, at $t = 160\mathrm{s}$. The numerical resolution is $\Delta x = 0.25\mathrm{m}$. (*a*) Colour map of flow depth. (*b*) Sum of the flow depth, projected vertically, H/γ and the vertical change in bed height $\Delta b = b|_{t=160\mathrm{s}} - b|_{t=0\mathrm{s}}$, within the self-channelised region [outlined by the dashed grey rectangle in (*a*)]. Points in the flow that lie below (above) the initial bed height are coloured blue (orange). The colour scale is linear, either side of zero. The solid blue and red dashed contours bound regions that are net erosive and net depositional: they show $\Delta b = -0.1\mathrm{m}$ and $0.1\mathrm{m}$ respectively. The range of change in bed height over this area is between $-1.7\mathrm{m}$ and $+1.1\mathrm{m}$ (to 2 s. f.). (*c*) Flow depth along the centreline interval indicated by the grey dashed line in (*a*).

where $\xi = y/w_p(x)$, with $w_p(x)$ denoting the width of the inundated region and C_H, C_w, Λ are constants given by

$$C_H = \left(\frac{4Q^2 \sin\vartheta}{3\pi\Lambda^2} \right)^{1/4}, \quad C_w = \left(\frac{16C_H}{3\sin\vartheta} \right)^{1/2}, \quad \Lambda = \left(g\sin\vartheta\cos^2\vartheta \right)^{1/2}. \qquad (4.8a\text{--}c)$$

Contours of these asymptotic solutions are included in Fig. 4, plotted with dashed black lines. In both cases, in the interior of the solution these align almost perfectly with the corresponding contours of the simulated depth field, validating the numerical results.

(ii) Steeper slopes.

At steeper slope angles, there are richer interactions between the flow and morphodynamics. In Fig. 6(*a*), we plot contours of flow depth for a flow on an initially constant $20°$ slope after 160s. We observe the flow splitting into two distinct regimes. Immediately downstream of the source, the flow is confined within a channel that it has excavated from the bed, extending for roughly 100m (at the time of the plotted snapshot). Detail of the morphodynamics in this region is given in Fig. 6(*b*). Points coloured blue in this plot lie below the original bed elevation and thus indicate flow within deeply eroded regions, whose lateral slopes constrain the material. This 'self-channelised' region grows deeper and longer in time, as more of the bed is removed. Further downstream, there is a region of deposit formed by some of the eroded sediment, followed by a longer, unconfined spreading flow. The flow front is travelling faster than the downstream expansion of the self-channelised region, which explains why most of the flow is unconfined at this point. The downstream flow does not erode or deposit a significant amount of sediment, indicating that it is in approximate morphodynamic equilibrium. However, because it is propagating on a steep slope, the flow is nonetheless vulnerable to the classical roll wave instability [64–67], the emergence of which can be seen around $x \gtrsim 500\mathrm{m}$. A one-dimensional cross-section of the free surface waves that the flow generates is plotted in Fig. 6(*c*).

The difference in behaviour between the two regimes may be understood by referring back to Fig. 5. Its dotted red curves show the maximum erosion rates for the flow inside and outside the channelised region [taken to be the area of Fig. 6(*b*)]. Flow within the channel reaches high speeds that cause the erosion rate to exceed the maximum deposition rate. This leads to sustained
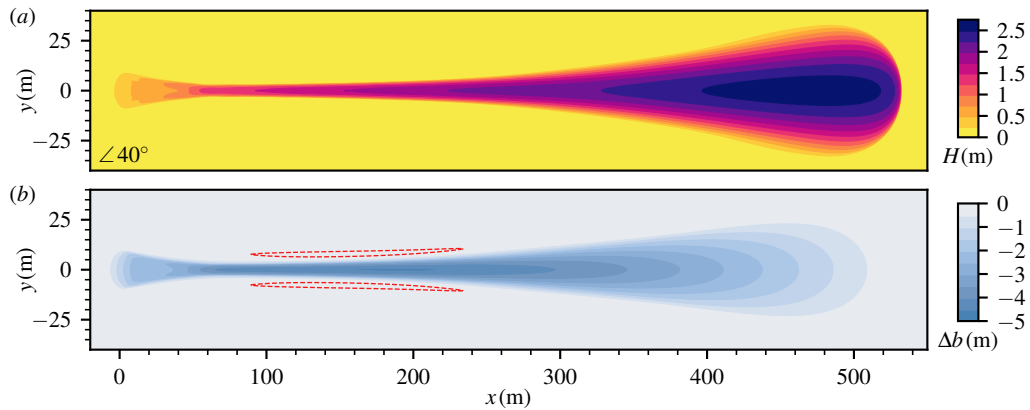
Figure 7. A 'super-erosive' flow state at $t = 80\mathrm{s}$. The initial bed is a constant slope at $40°$ inclination, fed by a $50\mathrm{m}^3/\mathrm{s}$ point source flux at the origin. The grid resolution is $\Delta x = 0.25\mathrm{m}$. (*a*) Contours of flow depth. (*b*) Bed elevation change $\Delta b = b|_{t=80\mathrm{s}} - b_{t=0\mathrm{s}}$. Blue filled contours indicate regions of net erosion. Dashed red contours are regions within which net deposition exceeds $+0.1\mathrm{m}$. The maximum deposition in these regions is $+0.22\mathrm{m}$ (2 s. f.).

erosion and the consequent accumulation of sediment concentration in the eroding region, which is advected downstream. As the sediment propagates away from the source, its concentration diminishes and flow speeds are reduced, so eventually $D > E$, leading to the formation of a deposit. The flow that spreads further downstream reaches a dilute morphodynamic equilibrium, analogous to what is observed in the $1°$ and $5°$ slopes (see Fig. 4).

At yet higher slope angles, a new state emerges, in which erosion occurs so rapidly that the expansion of eroded region matches the flow front velocity. In Fig. 7(*a,b*), we plot contours of the flow depth and the change in bed height, for a solution at initial slope angle $40°$, after $80\mathrm{s}$. The striking teardrop shape of the inundated area is almost entirely contained within a region that is net erosive. Indeed, so much material is entrained that the flow attains the maximum sediment concentration $\bar{\psi} = \psi_b$ throughout this region. Due to the hindered settling law, this renders deposition essentially nonexistent, save for some narrow bands at the edges of the flow. While the flow is initially driven by the source flux, its volume quickly becomes dominated by entrained material. In fact, once established, the state is self-perpetuating and continues to propagate even if the source is turned off. This is possible due to an erosive 'domino effect'—rapid erosion liberates gravitational potential energy from the bed, which accelerates the front and increases the erosion rate in turn. The principal restoring force available, basal drag, is unable to match the accumulated forcing from the slope-parallel weight, which grows more rapidly as the flow progresses.

(b) Flow between two uniform slopes.

We conclude this section with an example of flow that propagates from a steep slope to a shallower one, as typically occurs when debris flows are initiated on mountainsides. Specifically, we consider the following initial surface:

$$b(x, y, 0) = -\frac{(s_1 + s_2)x}{2} + \frac{(s_1 - s_2)\lambda}{2} \log\left[\cosh\left(\frac{x}{\lambda}\right)\right]. \qquad (4.9)$$

This constructs a slope that transitions between gradients s_1 upstream ($x \to -\infty$) and s_2 downstream ($x \to \infty$), over a characteristic length scale λ.

In Fig. 8, we present four progressive snapshots of a simulation with $s_1 = \tan(20°)$, $s_2 = \tan(2°)$ and $\lambda = 5\mathrm{m}$, initiated $150\mathrm{m}$ upstream from the change in slope. The flow shares properties observed in both the steep and gentle constant slope simulations of the previous subsection. In the first
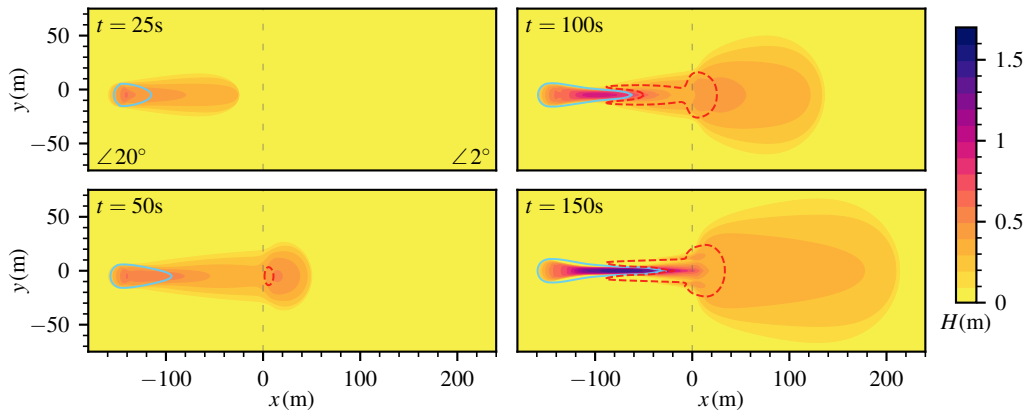
Figure 8. Simulated flow on an initially constant $20°$ slope, that smoothly transitions to an initially constant $2°$ slope downstream. The centreline of this transition, at $x = 0$m, is shown in dashed grey. The flow is fed by a $50\mathrm{m}^3/\mathrm{s}$ point source flux at $(x, y) = (-150\mathrm{m}, 0\mathrm{m})$. Four filled contour maps of flow depth are plotted, at times $t = 25$s, 50s, 100s and 150s, as indicated. Solid blue contours enclose regions where erosion has reduced the bed elevation by more than 0.1m and red dashed contours indicate regions where net deposits exceed 0.1m. The grid resolution is $\Delta x = 0.25$m.

snapshot, at $t = 25$s, the flow has progressed rapidly. It has eroded some of the bed near the source, but not enough to confine the bulk of the current. At $t = 50$s, the flow has reached the milder slope, slowing the speed of the front and causing it to expand laterally. When the flow decelerates, this the reduces erosion rate, which in turn reduces the sediment carrying capacity of the flow. This leads to the creation of a deposit formed from some of the flow material excavated upstream. At $t = 100$s, the upstream erosional region is now deep enough for the flow to self-channelise, as observed above in the $20°$ simulation presented in Fig. 6 [see especially panel (*b*)]. As the simulation progresses to $t = 150$s, the erosional region deepens and gradually invades its own deposit. Far downstream, the flow has matured into a steady spreading equilibrium, of the kind observed in Fig. 4.

5. Discussion

In this paper, new depth-averaged governing equations were derived for morphodynamic shallow flows with a suspended sediment phase, which are valid for weakly curved topographies that feature an arbitrary range of basal gradients. This advance is crucial for future modelling studies in geophysical settings, where flows transition from very steep slopes onto gentler ones, such as debris flows initiated in mountainous regions [1] and volcanic flows [4,5]. Our equations are formulated from a general perspective that allows them to be specialised to a variety of settings, from dilute suspensions to mudflows and granular media, by specifying appropriate modelling closures. Moreover, they are far simpler than shallow models that incorporate the full effects of arbitrary surface curvature making them more tractable to simulate from the perspective of practical natural hazards assessment.

To this end, we developed and implemented a strategy for numerically solving the governing equations using an operator splitting approach that enables existing non-morphodynamic finite volume codes to be extended to include coupled bed evolution and a sediment phase. Desirable properties of the underlying shallow flow scheme may be retained this way—in our implementation (which extends methods reported in Ref. [56]) this includes exact numerical integration of steady states (well balancing), though some new steps in the scheme were necessary to accommodate this for morphodynamic flows, as detailed in Sec. 3. In this way, there is the potential to extend the operator-split morphodynamic scheme, as and when technical advances in shallow water methods become available. Though it might also be anticipated that

mass conservation should follow automatically (given that finite volume schemes are typically conservative by construction), we have had to resolve multiple subtleties involving the geometric transformation of volume elements and book-keeping of morphodynamic transfers between the bed and flow. Failure to take similar precautions may result in schemes that are systematically biased towards gaining or losing mass in context-dependent ways.

Our numerical implementation incorporates terms corresponding to turbulent momentum diffusivity, given in Eq. (2.31). Though often neglected in these models (Ref. [10] is a rare exception), this physics offers a way to ensure that the governing equations are well posed when integrated as an initial-value problem [28]. Our demonstration of the problem in Fig. 3 highlights the issue that faces unregularised schemes: finer discretisation leads to divergence of the numerically computed flows, rather than convergence. The severe instability that underpins the phenomenon only emerges at length scales shorter than grid resolutions typically used in practical simulations, which suggests a possible reason why the issue may have previously gone unnoticed in susceptible models. This highlights the necessity of robust convergence testing for morphodynamic models, especially when they may be used in practical hazards assessment and other sensitive applications. In addition to eddy diffusivity, the issue may be alleviated by adding bed load fluxes to the morphodynamic equation (which some models already feature [11,14,16,42]), though we note that well posedness is contingent on the choice of flux closure in this case [27,28].

The results presented in Sec. 4 as demonstrations of the model in operation merit some discussion in their own right. Though the closures we have adopted are somewhat simplified, they are nonetheless sufficient to offer some phenomenological insight into the basic interactions of shallow flows with the processes of erosion and deposition. Our survey of flows spreading from point flux sources on initially constant slopes reveals some interesting flow regimes. On mild slopes, basal drag is sufficiently weak that sediment entrainment adopts a dynamic balance with the deposition rate throughout the flow bulk, thereby nullifying the net effect of morphodynamics. We demonstrated that this is the consequence of an attracting fixed point in the bed evolution equation that always exists when erosion lies below a certain threshold. Within this regime, it is possible to construct similarity solutions for the flow that reach very good agreement with the numerical simulations. In Appendix B, we derived formulae for these solutions that encompass a broad class of basal drag closures. These may prove valuable (as they have done here) for testing numerical schemes, since analytical solutions are usually difficult to obtain for morphodynamic flows.

On steeper slopes, which drive higher flow speeds, the entrainment rate is able to exceed the maximum rate of sediment deposition, leading to substantial erosion. The bifurcation to this state can be quite dramatic, since sediment uptake enhances the local solids concentration, which reduces the deposition rate via the effect of hindered settling and thereby increases net erosion in turn. In this regime, spreading flows cut grooves in the bed that are preferentially focussed along their centreline (where flow speed is maximised, in these simple states). These grooves ultimately grow into deep channels, leading to flow self-confinement. In a related, but more extreme regime observed at higher slope angles, the flow develops into a highly concentrated self-accelerating front, due to a positive feedback loop between gravitational forcing and entrainment, which outscales the restorative influence of drag. To our knowledge, such a phenomenon has not previously been identified in debris flows. However, it shares clear parallels with observations of self-accelerating turbidity currents, whose entrainment of basal sediment has been ascribed as a direct mechanism for their sustenance [68–70]. In our simulations, the self-accelerating states grow rapidly and without bound. In natural applications, this growth will instead be limited by the finite extent of steep slopes and the availability of readily erodible material, which is bounded because the subsurface typically consists of an erodible layer of soils and unconsolidated sediment underlain by much less erodible bedrock [71]. Nevertheless, it could be that these processes are transiently responsible for observations of particularly intense erosion from debris flows [1,72,73].

While we would anticipate some quantitative changes in our results if our simplified closures were substituted with empirical formulae fitted to real scenarios, we expect the qualitative

phenomena described here to be robust. Relatedly, we concluded our results with a brief example flow propagating from a steeper to a shallower slope. We note that most of its qualitative features could have been anticipated in advance, by referring to flow regimes already identified in the constant slope cases. This suggests that insights gleaned from simple morphodynamic flows may be useful for understanding dynamics on more complex terrains.

A. Lake at rest

Here, we show that time derivatives computed by our numerical method are exactly zero for 'lake-at-rest' initial conditions, which satisfy Eq. (2.27). We denote by η_c and $\bar{\rho}_c$, the spatially-constant values of η and $\bar{\rho}$ respectively. As discussed above, the only nontrivial cases to consider are the momentum equations, for which we must verify that the discretised forms of the hydrostatic pressure gradient must exactly balance. These are given in Eqs. (3.12) and (3.13). Therefore, for the $\bar{u}$-momentum equation, we must verify that

$$\left[1 + (b_y)_{i,j}^2\right] \frac{\partial \zeta}{\partial x}(x_i, y_j) - (b_x)_{i,j}(b_y)_{i,j}\frac{\partial \zeta}{\partial y}(x_i, y_j) = -\bar{\rho}_c g(\eta_c - b_{i,j})(b_x)_{i,j}, \tag{A 1}$$

where $\zeta(x_i, y_j) = \frac{1}{2}\bar{\rho}_c g(\eta_c - b_{i,j})^2$. Using Eqs. (3.10a,b) and (3.11a–c), we compute

$$\frac{\partial \zeta}{\partial x}(x_i, y_j) = \frac{\bar{\rho}_c g}{2\Delta x}\left[(\eta_c - b_{i+1/2,j})^2 - (\eta_c - b_{i-1/2,j})^2\right] \tag{A 2a}$$

$$= -\bar{\rho}_c g\left[(2\eta_c - b_{i-1/2,j} - b_{i+1/2,j})\frac{(b_{i+1/2,j} - b_{i-1/2,j})}{2\Delta x}\right] \tag{A 2b}$$

$$= -\bar{\rho}_c g(\eta_c - b_{i,j})(b_x)_{i,j}. \tag{A 2c}$$

Therefore, we must show that the remaining terms on the left-hand side of Eq. (A 1) sum to zero. This is clear after computing

$$(b_y)_{i,j}\frac{\partial \zeta}{\partial x}(x_i, y_j) = \frac{\bar{\rho}_c g}{2\Delta x \Delta y}(b_{i,j+1/2} - b_{i,j-1/2})\left[(\eta_c - b_{i+1/2,j})^2 - (\eta_c - b_{i-1/2,j})^2\right] \tag{A 3a}$$

$$= \frac{\bar{\rho}_c g}{2\Delta x \Delta y}(b_{i+1/2,j} - b_{i-1/2,j})\left[(\eta_c - b_{i,j+1/2})^2 - (\eta_c - b_{i,j-1/2})^2\right] \tag{A 3b}$$

$$= (b_x)_{i,j}\frac{\partial \zeta}{\partial y}(x_i, y_j), \tag{A 3c}$$

and multiplying both sides by $(b_y)_{i,j}$. To swap the indices between Eqs. (A 3a) and (A 3b), we rearranged the terms and used the fact that $b_{i+1/2,j} + b_{i-1/2,j} = b_{i,j+1/2} + b_{i,j-1/2}$. The balances for the $\bar{v}$-momentum equation are obtained by the same reasoning due to symmetry.

B. Similarity solutions for mild constant slopes

If the morphodynamics processes are in equilibrium, then $M = 0$ and the bulk density $\bar{\rho}$ is constant. Since motion is primarily downslope, we expect $\bar{u} \gg \bar{v}$ and therefore, $|\bar{\boldsymbol{u}}| = \bar{u}/\cos(\vartheta)$ to leading order. Furthermore, we seek solutions for steady flow, whose spatial variation is sufficiently small that the effects of eddy viscosity may be neglected. These assumptions lead to considerable simplifications of the governing equations (3.1a)–(3.3e). The dominant balances in the momentum equations become

$$gH\sin(\vartheta) = \frac{\tau_b}{\bar{\rho}}, \quad \text{and} \quad gH\frac{\partial H}{\partial y} = -\frac{\tau_b}{\bar{\rho}}\frac{\bar{v}}{\bar{u}}. \tag{A 1a,b}$$

For many drag formulations, Eq. (A 1a) may be rearranged to give $\bar{u} = \Lambda H^m$, where Λ and m are constants particular to the choice of τ_b (e.g. see [74]). This includes the Chézy drag closure employed above [Eq. (4.1)], for which $m = 1/2$. Substituting the general expression into the mass conservation equation gives

$$\frac{\partial}{\partial x}(H^{m+1}) = \frac{1}{\sin(\vartheta)}\frac{\partial}{\partial y}\left(H^{m+1}\frac{\partial H}{\partial y}\right). \tag{A 2}$$

This is subject to a flux condition

$$\int_{-w_p(x)}^{w_p(x)} H^{m+1}\,\mathrm{d}y = \frac{Q}{\Lambda}, \tag{A 3}$$

for all $x > 0$ (i.e. downstream of the source), where $w_p(x)$ denotes the distance from the symmetry line $y = 0$ to the perimeter of the wetted region in the y-direction.

Since there are no external length scales present in the system, we expect the asymptotic solutions to be self-similar. The essential scalings present in Eqs. (A 2) and (A 3) are $H/w_p^2 \sim \sin(\vartheta)/x$ and $H^{m+1} \sim Q/(\Lambda w_p)$. These motivate the following ansatz

$$H(x,\xi) = C^2\left[\frac{Q^2}{\Lambda^2}\frac{\sin(\vartheta)}{x}\right]^{\frac{1}{2m+3}}F(\xi), \quad w_p(x) = C\left[\frac{Q}{\Lambda}\left(\frac{x}{\sin(\vartheta)}\right)^{m+1}\right]^{\frac{1}{2m+3}}, \tag{A 4a,b}$$

where $\xi = y/w(x)$ and C is a constant to be determined. On substituting these into Eq. (A 2), we arrive at an ordinary differential equation for the cross-stream dependence,

$$-\frac{m+1}{2m+3}\frac{\mathrm{d}}{\mathrm{d}\xi}\left[\xi F(\xi)^{m+1}\right] = \frac{\mathrm{d}}{\mathrm{d}\xi}\left[F(\xi)^{m+1}\frac{\mathrm{d}F}{\mathrm{d}\xi}\right]. \tag{A 5}$$

By integrating and applying the boundary condition $F(\pm 1) = 0$, we find that $F(\xi) = F_0(1-\xi^2)$, where $F_0 = \frac{m+1}{2(2m+3)}$. Then, by evaluating Eq. (A 3), C may be determined to complete the solutions, which are given compactly as

$$H(x,\xi) = \left[\frac{F_0 Q^2}{\Upsilon^2 \Lambda^2}\frac{\sin(\vartheta)}{x}\right]^{\frac{1}{2m+3}}(1-\xi^2), \quad w(x) = \left[\frac{Q}{\Upsilon\Lambda}\left(\frac{x}{F_0\sin(\vartheta)}\right)^{m+1}\right]^{\frac{1}{2m+3}}, \tag{A 6a,b}$$

where $\Upsilon = \int_0^\pi \sin^{2m+3}(\phi)\,\mathrm{d}\phi$. To specialise these to a particular drag law, one simply specifies m.

References

1. Jakob M, Hungr O. 2005 *Debris-flow hazards and related phenomena* vol. 739. Springer.
2. Auker MR, Sparks RSJ, Siebert L, Crosweller HS, Ewert J. 2013 A statistical analysis of the global historical volcanic fatalities record. *J. Applied Volc.* **2**, 2.
3. Dowling CA, Santi PM. 2014 Debris flows and their toll on human life: a global analysis of debris-flow fatalities from 1950 to 2011. *Nat. Hazards* **71**, 203–227.
4. Pierson TC, Janda RJ, Thouret JC, Borrero CA. 1990 Perturbation and melting of snow and ice by the 13 November 1985 eruption of Nevado del Ruiz, Colombia, and consequent mobilization, flow and deposition of lahars. *J. Volcanol. Geotherm. Res.* **41**, 17 – 66.

5. Scott KM, Vallance JW, Kerle N, Luis Macías J, Strauch W, Devoli G. 2005 Catastrophic precipitation-triggered lahar at Casita volcano, Nicaragua: occurrence, bulking and transformation. *Earth Surf. Proc. Land.* **30**, 59–79.

6. Capart H, Young DL. 1998 Formation of a jump by the dam-break wave over a granular bed. *J. Fluid Mech.* **372**, 165–187.

7. Brufau P, Garcia-Navarro P, Ghilardi P, Natale L, Savi F. 2000 1D mathematical modelling of debris flow. *J. Hydraul. Res.* **38**, 435–446.

8. Egashira S, Honda N, Itoh T. 2001 Experimental study on the entrainment of bed material into debris flow. *Phys. Chem. Earth Pt. C* **26**, 645–650.

9. Cao Z, Pender G, Wallis S, Carling P. 2004 Computational dam-break hydraulics over erodible sediment bed. *J. Hydraul. Eng.* **130**.

10. Simpson G, Castelltort S. 2006 Coupled model of surface water flow, sediment transport and morphological evolution. *Comput. Geosci.* **32**, 1600–1614.

11. Wu W, Wang SS. 2007 One-dimensional modeling of dam-break flow over movable beds. *J. Hydraul. Eng.* **133**, 48–58.

12. Zech Y, Soares-Frazão S, Spinewine B, Le Grelle N. 2008 Dam-break induced sediment movement: Experimental approaches and numerical modelling. *J. Hydraul. Res.* **46**, 176–190.

13. Armanini A, Fraccarollo L, Rosatti G. 2009 Two-dimensional simulation of debris flows in erodible channels. *Comput. Geosci.* **35**, 993–1006.

14. Murillo J, García-Navarro P. 2010 An Exner-based coupled model for two-dimensional transient flow over erodible bed. *J. Comput. Phys.* **229**, 8704–8732.

15. Greco M, Iervolino M, Leopardi A, Vacca A. 2012 A two-phase model for fast geomorphic shallow flows. *Int. J. Sediment Res.* **27**, 409–425.

16. Benkhaldoun F, Elmahi I, Sari S, Seaïd M. 2013 An unstructured finite-volume method for coupled models of suspended sediment and bed load transport in shallow-water flows. *Int. J. Numer. Meth. Fl.* **72**, 967–993.

17. Swartenbroekx C, Zech Y, Soares-Frazão S. 2013 Two-dimensional two-layer shallow water model for dam break flows with significant bed load transport. *Int. J. Numer. Meth. Fl.* **73**, 477–508.

18. Li J, Cao Z, Hu K, Pender G, Liu Q. 2018 A depth-averaged two-phase model for debris flows over erodible beds. *Earth Surf. Proc. Land.* **43**, 817–839.

19. Pudasaini SP, Krautblatter M. 2021 The mechanics of landslide mobility with erosion. *Nat. Commun.* **12**, 6793.

20. Soares-Frazao S, Canelas R, Cao Z, Cea L, Chaudhry HM, Die Moran A, El Kadi K, Ferreira R, Cadórniga IF, Gonzalez-Ramirez N, Greco M, Huang W, Imran J, Le Coz J, Marsooli R, Paquier A, Pender G, Pontillo M, Puertas J, Spinewine B, Swartenbroekx C, Tsubaki R, Villaret C, Wu W, Yue Z, Zech Y. 2012 Dam-break flows over mobile beds: experiments and benchmark tests for numerical models. *J. Hydraul. Res.* **50**, 364–375.

21. Liu J, Nakatani K, Mizuyama T. 2013 Effect assessment of debris flow mitigation works based on numerical simulation by using Kanako 2D. *Landslides* **10**, 161–173.

22. Guan M, Wright NG, Sleigh PA, Carrivick JL. 2015 Assessment of hydro-morphodynamic modelling and geomorphological impacts of a sediment-charged jökulhlaup, at Sólheimajökull, Iceland. *J. Hydrol.* **530**, 336–349.

23. Santillán D, Cueto-Felgueroso L, Sordo-Ward A, Garrote L. 2020 Influence of erodible beds on shallow water hydrodynamics during flood events. *Water* **12**, 3340.

24. Jenkins LT, Creed MJ, Tarbali K, Muthusamy M, Trogrlić RŠ, Phillips JC, Watson CS, Sinclair HD, Galasso C, McCloskey J. 2023 Physics-based simulations of multiple natural hazards for risk-sensitive planning and decision making in expanding urban regions. *International J. Disast. Risk Re.* **84**, 103338.

25. Haugen ED, Kaynia AM. 2008 Vulnerability of structures impacted by debris flow. In *Landslides and Engineered Slopes. From the Past to the Future* pp. 403–410. CRC Press.

26. Gentile R, Cremen G, Galasso C, Jenkins LT, Manandhar V, Menteşe EY, Guragain R, McCloskey J. 2022 Scoring, selecting, and developing physical impact models for multi-hazard risk assessment. *Int. J. Disast. Risk Re.* **82**, 103365.

27. Chavarrías V, Stecca G, Blom A. 2018 Ill-posedness in modeling mixed sediment river morphodynamics. *Adv. Water Res.* **114**, 219–235.

28. Langham J, Woodhouse MJ, Hogg AJ, Phillips JC. 2021 Linear stability of shallow morphodynamic flows. *J. Fluid Mech.* **916**.

29. Iverson RM, Ouyang C. 2015 Entrainment of bed materials by Earth-surface mass flows: Review and reformulation of depth-integrated theory. *Rev. Geophys.* **53**.

30. Dressler RF. 1978 New nonlinear shallow-flow equations with curvature. *J. Hydraul. Res.* **16**, 205–222.

31. Berger RC, Carey GF. 1998 Free-surface flow over curved surfaces: Part I: Perturbation analysis. *Int. J. Numer. Meth. Fl.* **28**, 191–200.

32. Gray JMNT, Wieland M, Hutter K. 1999 Gravity-driven free surface flow of granular avalanches over complex basal topography. *Proc. Roy. Soc. Lond. A. Mat.* **455**, 1841–1874.

33. Keller JB. 2003 Shallow-water theory for arbitrary slopes of the bottom. *J. Fluid Mech.* **489**, 345–348.

34. Bouchut F, Mangeney-Castelnau A, Perthame B, Vilotte J. 2003 A new model of Saint Venant and Savage-Hutter type for gravity driven shallow water flows. *C. R. Math.* **336**, 531–536.

35. Bouchut F, Westdickenberg M. 2004 Gravity driven shallow water models for arbitrary topography. *Commun. Math. Sci.* **2**, 359–389.

36. Peruzzetto M, Mangeney A, Bouchut F, Grandjean G, Levy C, Thiery Y, Lucas A. 2021 Topography curvature effects in thin-layer models for gravity-driven flows without bed erosion. *J. Geophys. Res. Earth Surf.* **126**, e2020JF005657.

37. Bouchut F, Fernandez-Nieto ED, Mangeney A, Lagrée PY. 2008 On new erosion models of Savage–Hutter type for avalanches. *Acta Mech.* **199**, 181–208.

38. Yue Z, Cao Z, Li X, Che T. 2008 Two-dimensional coupled mathematical modeling of fluvial processes with intense sediment transport and rapid bed evolution. *Sci. China Ser. G* **51**, 1427–1438.

39. Xia J, Lin B, Falconer RA, Wang G. 2010 Modelling dam-break flows over mobile beds using a 2D coupled approach. *Adv. Water Resour.* **33**, 171–183.

40. Canelas R, Murillo J, Ferreira RML. 2013 Two-dimensional depth-averaged modelling of dam-break flows over mobile beds. *J. Hydraul. Res.* **51**, 392–407.

41. Liu X, Mohammadian A, Kurganov A, Sedano JAI. 2015 Well-balanced central-upwind scheme for a fully coupled shallow water system modeling flows over erodible bed. *J. Comput. Phys.* **300**, 202–218.

42. Liu X, Beljadid A. 2017 A coupled numerical model for water flow, sediment transport and bed erosion. *Comput. Fluids* **154**, 273–284.

43. Martínez-Aranda S, Murillo J, García-Navarro P. 2019 A 1D numerical model for the simulation of unsteady and highly erosive flows in rivers. *Comput. Fluids* **181**, 8–34.

44. Chertock A, Kurganov A, Wu T. 2020 Operator splitting based central-upwind schemes for shallow water equations with moving bottom topography. *Commun. Math. Sci.* **18**.

45. Kurganov A, Petrova G. 2007 A second-order well-balanced positivity preserving central-upwind scheme for the Saint-Venant system. *Commun. Math. Sci.* **5**, 133–160.

46. Savage SB, Hutter K. 1989 The motion of a finite mass of granular material down a rough incline. *J. Fluid Mech.* **199**, 177–215.

47. Iverson RM. 1997 The physics of debris flows. *Rev. Geophys.* **35**, 245–296.

48. Hogg AJ, Pritchard D. 2004 The effects of hydraulic resistance on dam-break and other shallow inertial flows. *J. Fluid Mech.* **501**, 179–212.

49. Kerswell RR. 2005 Dam break with Coulomb friction: A model for granular slumping?. *Phys. Fluids* **17**, 057101.

50. Joseph DD, Saut JC. 1990 Short-wave instabilities and ill-posed initial-value problems. *Theor. Comp. Fluid Dyn.* **1**, 191–227.

51. Barnhart KR, Jones RP, George DL, McArdell BW, Rengers FK, Staley DM, Kean JW. 2021 Multi-model comparison of computed debris flow runout for the 9 January 2018 Montecito, California post-wildfire event. *J. Geophys. Res. Earth Surf.* **126**, e2021JF006245.

52. Strang G. 1968 On the construction and comparison of difference schemes. *SIAM J. Numer. Anal.* **5**, 506–517.

53. LeVeque RJ. 2002 *Finite volume methods for hyperbolic problems* vol. 31. Cambridge University Press.

54. Kurganov A, Levy D. 2002 Central-upwind schemes for the Saint-Venant system. *ESAIM: M2AN* **36**, 397–425.

55. Kurganov A. 2018 Finite-volume schemes for shallow-water equations. *Acta Numer.* **27**, 289–351.

56. Chertock A, Cui S, Kurganov A, Wu T. 2015 Well-balanced positivity preserving central-upwind scheme for the shallow water system with friction terms. *Int. J. Numer. Meth. Fl.* **78**, 355–383.

57. Chertock A, Kurganov A. 2008 A second-order positivity preserving central-upwind scheme for chemotaxis and haptotaxis models. *Numer. Math.* **111**, 169–205.
58. Kurganov A, Tadmor E. 2000 New high-resolution central schemes for nonlinear conservation laws and convection–diffusion equations. *Journal Comput. Phys.* **160**, 241–282.
59. Chertock A, Cui S, Kurganov A, Wu T. 2015 Steady state and sign preserving semi-implicit Runge-Kutta methods for ODEs with stiff damping term. *SIAM J. Numer. Anal.* **53**, 2008–2029.
60. Lajeunesse E, Malverti L, Charru F. 2010 Bed load transport in turbulent flow at the grain scale: Experiments and modeling. *J. Geophys. Res.-Earth* **115**.
61. Richardson JF, Zaki WN. 1954 Sedimentation and fluidisation. Part 1. *Trans. Inst. Chem. Eng.* **32**.
62. Spearman J, Manning AJ. 2017 On the hindered settling of sand-mud suspensions. *Ocean Dynam.* **67**, 465–483.
63. Bonnecaze RT, Lister JR. 1999 Particle-driven gravity currents down planar slopes. *J. Fluid Mech.* **390**, 75–91.
64. Jeffreys H. 1925 The flow of water in an inclined channel of rectangular section. *Phil. Mag.* **49**, 793–807.
65. Cornish V. 1934 *Ocean waves and kindred geophysical phenomena*. Cambridge University Press.
66. Dressler RF. 1949 Mathematical solution of the problem of roll-waves in inclined open channels. *Commun. Pur. Appl. Math.* **2**, 149–194.
67. Needham DJ, Merkin JH. 1984 On roll waves down an open inclined channel. *P. Roy. Soc. Lond. A Mat.* **394**, 259–278.
68. Parker G. 1982 Conditions for the ignition of catastrophically erosive turbidity currents. *Mar. Geol.* **46**, 307–327.
69. Parker G, Fukushima Y, Pantin HM. 1986 Self-accelerating turbidity currents. *J. Fluid Mech.* **171**, 145–181.
70. Blanchette F, Strauss M, Meiburg E, Kneller B, Glinsky ME. 2005 High-resolution numerical simulations of resuspending gravity currents: Conditions for self-sustainment. *J. Geophys. Res.–Oceans* **110**.
71. Heimsath AM, DiBiase RA, Whipple KX. 2012 Soil production limits and the transition to bedrock-dominated landscapes. *Nat. Geosci.* **5**, 210–214.
72. Stock JD, Dietrich WE. 2006 Erosion of steepland valleys by debris flows. *Geol. Soc. Am. Bull.* **118**, 1125–1148.
73. Shen P, Zhang L, Wong HF, Peng D, Zhou S, Zhang S, Chen C. 2020 Debris flow enlargement from entrainment: A case study for comparison of three entrainment models. *Eng. Geol.* **270**, 105581.
74. Langham J, Hogg AJ. 2022 General linear stability properties of monoclinal shallow waves. *Phys. Rev. Fluids* **7**, 053902.